Earth System
Science
Data

Development of a High-Resolution Integrated Emission Inventory of Air Pollutants for China

Nana Wu[1], Guannan Geng[2,3*], Ruochong Xu[1], Shigan Liu[1], Xiaodong Liu[2], Qinren Shi[2], Ying Zhou[4], Yu Zhao[5], Huan Liu[2,3], Yu Song[6], Junyu Zheng[7], and Qiang Zhang[1]

[1]Ministry of Education Key Laboratory for Earth System Modeling, Department of Earth System Science, Tsinghua University, Beijing 100084, China
[2]State Key Joint Laboratory of Environment Simulation and Pollution Control, School of Environment, Tsinghua University, Beijing 100084, China
[3]State Environmental Protection Key Laboratory of Sources and Control of Air Pollution Complex, Beijing 100084, China
[4]Key Laboratory of Beijing on Regional Air Pollution Control, Faculty of Environment and Life, Beijing University of Technology, Beijing, 100124, China
[5]State Key Laboratory of Pollution Control and Resource Reuse and School of the Environment, Nanjing University, 163 Xianlin Rd., Nanjing, Jiangsu 210023, China
[6]State Key Joint Laboratory of Environmental Simulation and Pollution Control, College of Environmental Sciences and Engineering, Peking University, Beijing 100871, PR China
[7]Sustainable Energy and Environmental Thrust, The Hong Kong University of Science and Technology (Guangzhou), Guangzhou, 511458, China

Correspondence to: Guannan Geng (guannangeng@tsinghua.edu.cn)

Abstract. Constructing a highly-resolved comprehensive emission dataset for China is challenging due to limited availability of refined information for parameters in a unified bottom-up framework. Here, by developing an integrated modeling framework, we harmonized multi-source heterogeneous data including several up-to-date emission inventories at national and regional scale, and for key species and sources in China, to generate a 0.1 °resolution inventory for 2017. By source mapping, species mapping, temporal disaggregation, spatial allocation and spatial-temporal coupling, different emission inventories are normalized in terms of source categories, chemical species, and spatiotemporal resolutions. This achieves the coupling of multi-scale, high-resolution emission inventories with the MEIC (Multi-resolution Emission Inventory for China), forming a high-resolution INTegrated emission inventory of Air pollutants for China (i.e., INTAC). We find that the INTAC provides more accurate representations for emission magnitudes and spatiotemporal patterns. In 2017, China's emissions of SO_2, NO_x, CO, NMVOC, NH_3, PM_{10}, $PM_{2.5}$, BC, and OC are 12.3, 24.5, 141.0, 27.9, 9.2, 11.1, 8.4, 1.3 and 2.2 Tg, respectively. The proportion of point source emissions for SO_2, PM_{10}, NO_x, $PM_{2.5}$ increases from 7–19% in MEIC to 48–66% in INTAC, resulting in improved spatial accuracy, especially mitigating overestimations in densely populated areas. Compared to MEIC, INTAC reduced mean biases in simulated concentrations of major air pollutants by 2–14 μg/m³ across 74 cities against ground observations. The enhanced model performance by INTAC was particularly evident at finer grid resolutions. Our new dataset is accessible at https://doi.org/10.5281/zenodo.10459198 (Wu et al., 2024), and it will provide a solid data foundation for fine-scale atmospheric research and air quality improvement.

1 Introduction

In recent years, China has achieved remarkable progress in improving air quality and public health through the active implementation of clean air policies (Xiao et al., 2022; Zhang et al., 2019a; Liu et al., 2020; Zhang and Geng, 2019). To further unlock the potential of targeted clean air actions, there is an urgent need for an accurate and detailed depiction for emissions, encompassing their magnitudes and spatial-temporal patterns. Developing a reliable highly-resolved emission inventory for China is also crucial for studies of atmospheric chemistry and climate change (Zhang et al., 2019a; Geng et al., 2021; Cheng et al., 2021a).

The construction of high-resolution emission inventories for China poses significant challenges due to the diversity and complexity of emission sources and technology distributions. Additionally, the limited availability of localized measurements for emission factors (EFs) and source profiles, along with exact location of the emission facilities, further compounds the difficulties (Li et al., 2017a). The widely-used bottom-up approach involves the establishment of a unified framework that encompasses source categories, chemical speciation processes, spatial-temporal allocation profiles and emission estimation methods (Huang et al., 2021; An et al., 2021). However, achieving both wide coverage and high accuracy in compiling an emission inventory for China through this approach remains a formidable task for individual research institutions.

Comprehensive national-scale emission inventories developed using the unified framework typically provide extensive coverage of space, species and sectors (Li et al., 2017a; Li et al., 2023b), but tend to exhibit limitations in spatial accuracy (Wu et al., 2021; Zhou et al., 2017a; Zhao et al., 2015; Zheng et al., 2021). Previous studies have indicated that the spatial allocation in large-scale emission inventories rely on spatial proxies (e.g., population, road networks) rather than latitude-longitude coordinates of emission sources due to the unavailability of extensive spatial information (Zhang et al., 2009; Li et al., 2017b). The assumption of a linear correlation between emissions and spatial proxies might lead to an overestimation of emissions in urban areas, especially at scales finer than 0.25 ° (Zheng et al., 2017; Zheng et al., 2021; Wu et al., 2021). Biases introduced by the proxy-based method are found to be propagated as the grid size diminishes, resulting in uncertainties for chemical transport models (CTMs) (Zheng et al., 2017; Zheng et al., 2021).

Emission inventories focused on a specific region (Liu et al., 2018; An et al., 2021; Huang et al., 2021), sector (Deng et al., 2020; Chen et al., 2016; Zhou et al., 2017b) or key species (Li et al., 2021; Huang et al., 2012b; Wang et al., 2023) under the aforementioned unified framework demonstrate enhanced accuracy, but fail to achieve comprehensive coverage. These inventories assimilate substantial detailed foundational data from various statistical dataset, on-site measurements or surveys to represent real-world emission magnitudes, including energy consumption, removal efficiencies, and localized speciation profile (Liu et al., 2018; An et al., 2021; Huang et al., 2021). Innovative data, such as measurements from continuous emission monitoring systems (Tang et al., 2023; Bo et al., 2021; Wu et al., 2022), or methodologies like process-based models (Kang et al., 2016; Zhao et al., 2020) are implemented to enable a more accurate characterization of complex emission dynamics. Facility-level geographic location is incorporated to optimize the representation of spatial patterns (Liu et al., 2015a; Wu et

67 al., 2023; Wang et al., 2019). The reliability of these local-scale, sector- or species-specified inventories has been validated

68 against satellite and ground-based measurements (Zhang et al., 2021; Liu et al., 2016a; Zheng et al., 2019).

69 The other strategy for developing bottom-up emission inventories is commonly known as the integrated method. This method

70 consolidates emission datasets for various regions, species or sectors into a unified product, ensuring extensive coverage (Li

71 et al., 2017b). Taking advantage of existing inventories derived from localized data and advanced methods, the integrated

72 method facilitates the efficient generation of highly-resolved emission inventories at large scales. However, the heterogeneity

73 of different emission datasets presents challenges for the fusion, manifested in diverse data formats, sector categories, species,

74 spatial-temporal resolution. In recent years, there has been growing interest in adopting the integrated approach to enrich

75 inventories with local insights, particularly at the global (Janssens-Maenhout et al., 2015; Crippa et al., 2023) and Asian scales

76 (Zhang et al., 2009; Kurokawa et al., 2013; Li et al., 2023a; Li et al., 2017b). Researches on establishing integrated inventories

77 for China are constrained due to the inherent complexity and challenging accessibility of the data. These efforts are

78 concentrated in specific regions, such as the Yangtze River Delta (An et al., 2021).

79 In this work, with the support of several research institutions, we use an emission integration model to construct a high-

80 resolution integrated emission inventory at a spatial resolution of 0.1 ° for China in 2017, denoted as INTAC. The challenges

81 associated with coupling multi-source heterogeneous data are addressed through the implementation of an inventory

82 integration framework. Then, leveraging the strengths of inventories enriched with local knowledge, we compile a

83 comprehensive highly resolved emission product to enhance the accurate representation of emissions from crucial regions,

84 sectors and species. Finally, the improved accuracy of emission magnitude and spatial distribution is evaluated using

85 atmospheric chemistry models.

86 **2 Methodology and data**

87 Figure 1 illustrates the schematic diagram of the integration process of INTAC. We collect seven emission inventories—MEIC

88 developed by Tsinghua University (Li et al., 2017a; Zheng et al., 2018), the industrial point source emission inventory for

89 China by the MEIC team (Zheng et al., 2017; Zheng et al., 2021), the Yangtze River Delta (YRD) air pollutant emission

90 inventory led by Nanjing University (An et al., 2021; Zhou et al., 2017a), the Pearl River Delta (PRD) emission inventory by

91 Jinan University (Huang et al., 2021; Sha et al., 2021), the open biomass burning emission inventory in China by Peking

92 University (Song et al., 2009; Huang et al., 2012a; Yin et al., 2019; Liu et al., 2015b) , the shipping emission inventory in East

93 Asia by Tsinghua University (Liu et al., 2016b; Liu et al., 2019) , and the high-resolution ammonia emission inventory in

94 China (PKU-NH$_3$) by Peking University (Huang et al., 2012b; Kang et al., 2016). The details of these inventories and the

95 rationale for choosing them will be described in Sect. 2.1.
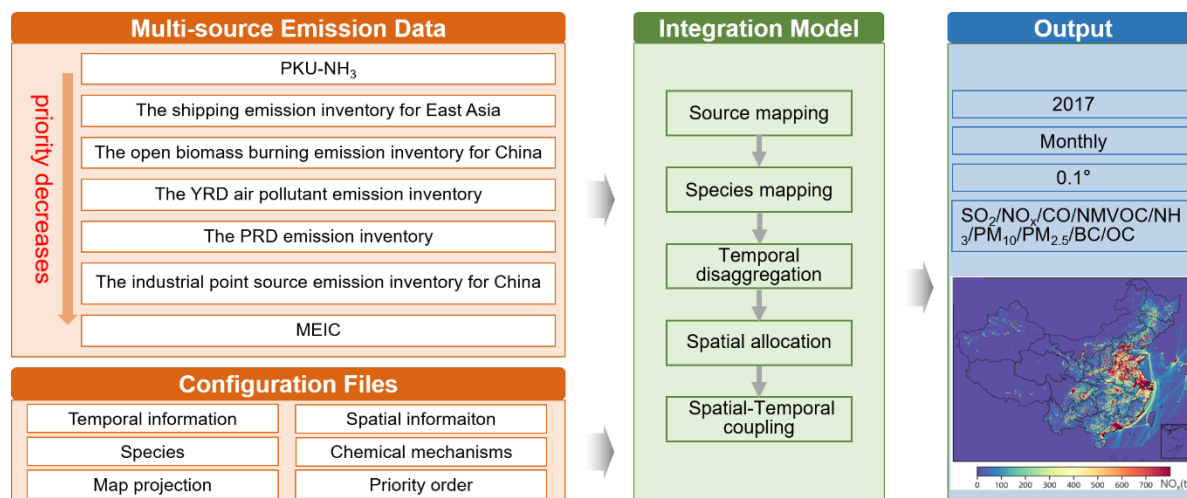
96 **Figure 1: Methodology framework of the INTAC inventory development.**

97 An integration model is then established to merge together emission inventories with different sectors, species, spatial-temporal

98 resolution and formats (i.e., point, area, and gridded forms). The integration process consists of five steps: source mapping,

99 species mapping, temporal disaggregation, spatial allocation, and spatial-temporal coupling, as detailed in Sect. 2.2. Based on

100 the priority order, multi-source emission inventories are assembled at the standardized specie, sector, and grid levels, yielding

101 a standardized data cube. Ultimately, an integrated emission inventory is created for China, featuring a resolution of 0.1 ° on a

102 monthly scale and covering nine air pollutants (i.e., SO_2, NO_x, CO, NMVOC, NH_3, PM_{10}, $PM_{2.5}$, BC, OC).

103 **2.1 Components of the integrated emission inventory INTAC**

104 Table 1 lists the essential details about the seven inventories and priority order utilized for integration. As the most widely

105 used anthropogenic emission inventory in China, MEIC functions as the default inventory in our integration, supplementing

106 missing data in other inventories. The remaining six emission inventories, demonstrating proficiency in specific species,

107 sectors, or regions, are coupled with MEIC to improve the representation of national emissions.

108 **Table 1: List of emission inventories collected in this work.**

Priority ranking	Emission inventory and developer	Year	Resolution	Region	Resolution	Species
1	PKU-NH$_3$ (Peking University)	1980–2017	Monthly	Mainland China	0.1°	NH$_3$
2	The shipping emission inventory for East Asia (Tsinghua University)	2017	Annually	East Asia	0.1°	SO$_2$/NO$_x$/CO/NMVOC/ PM$_{2.5}$/BC/OC
3	The open biomass burning emission inventory for China (Peking University)	1980–2017	Daily	Mainland China	~1km	SO$_2$/NO$_x$/CO/NMVOC/ NH$_3$/PM$_{10}$/PM$_{2.5}$/BC/OC
4	The PRD emission inventory (Jinan University)	2017	Monthly	PRD	0.05°	SO$_2$/NO$_x$/CO/NMVOC/ NH$_3$/PM$_{10}$/PM$_{2.5}$/BC/OC
5	The YRD emission inventory (Nanjing University/Shanghai Academy of Environmental Sciences/Jiangsu Provincial Academy of Environmental Science)	2017	Annually	YRD	0.1°	SO$_2$/NO$_x$/CO/NMVOC/ NH$_3$/PM$_{10}$/PM$_{2.5}$/BC/OC
6	The industrial point source emission inventory for China (Tsinghua University)	2012–2018	Monthly	Mainland China	~1km	SO$_2$/NO$_x$/CO/NMVOC/ NH$_3$/PM$_{10}$/PM$_{2.5}$/BC/OC
7	MEICv1.3 (Tsinghua University)	2008–2017	Monthly	Mainland China	0.25°	SO$_2$/NO$_x$/CO/NMVOC/ NH$_3$/PM$_{10}$/PM$_{2.5}$/BC/OC

109 **2.1.1 MEIC**

110 The integrated inventory INTAC is built upon MEIC, a comprehensive database with extensive coverage across time periods,

111 space, species, and sectors. Developed by Tsinghua University since 2010 (http://meicmodel.org.cn) (Li et al., 2017a; Zheng

112 et al., 2018), the MEIC provides monthly emissions for air pollutants and CO$_2$ in China from 1990 to the present at a resolution

113 of 0.25° × 0.25°. It caters to the demand for timely and accurate estimates of atmospheric emissions, gaining widespread

114 adoption by both domestic and international research institutions. We use 2017 emissions from MEIC v1.3 in this study.

115 MEIC employs several strategies to improve emission estimation parameters. This includes categorizing emission sources

116 across ~800 sectors, utilizing a technology- and big-data-driven approach for dynamic emission characterization, and

117 employing a localized emission factor database (Li et al., 2017a; Zheng et al., 2018). Emission estimates for power, on-road,
118 and residential sources are enhanced through the use of unit-level data (Liu et al., 2015a), county-level emission estimates
119 (Zheng et al., 2014), and integration of extensive household surveys (Peng et al., 2019), respectively. MEIC builds an database
120 encompassing temporal allocation profiles (ranging from yearly to monthly, daily, and hourly) (Li et al., 2017b), spatial
121 allocation proxies (from province to county, and further to grids) (Li et al., 2017b; Geng et al., 2017; Zheng et al., 2017), and
122 a speciation framework for NMVOC involving five mechanisms (CB-IV, CB05, SAPRC-07, SAPRC-99, and RADM2) (Li et
123 al., 2014) (Li et al., 2014) to support the development of model-ready gridded emissions.
124 Among the seven inventories, MEIC has the lowest priority, and is only considered when the other six cannot provide necessary
125 data for emissions from a specific city and source.

2.1.2 The industrial point source emission inventory for China

127 The proxy-based method used for spatial allocation in MEIC introduces biases in emission mapping, especially at kilometer
128 scale (Zheng et al., 2017; Zheng et al., 2021). To significantly reduce the uncertainty, we merged an industrial emission
129 inventory with detailed information on ~100,000 facilities into INTAC.
130 Compiled by Tsinghua University for the year 2013 (Zheng et al., 2021) and updated by the same research team for 2017, this
131 point-based inventory combines three databases investigated under the guidance of the Chinese government, offering a
132 comprehensive overview of industrial facilities. It includes details on locations, activity rates, production technology, end-of-
133 pipe pollution control devices, and other parameters. The facility-level, technology-based approach allows for dynamic
134 tracking of emission fluctuations resulting from technological advancements and tightening emission regulations. Crucially,
135 the use of facility geolocations rather than relying on spatial proxies like urban population enables the derivation of gridded
136 industrial data at a resolution of ~1 km. This approach significantly avoids misallocating emissions from rural to urban areas
137 at fine grids, as supported by previous studies demonstrating its effectiveness in mitigating simulated biases in air pollutant
138 concentrations within densely populated regions (Zheng et al., 2021). For temporal variations, it employs the same monthly
139 profiles as MEIC, including the production of various industrial goods or GDP, as outlined in Li et al. (2017b). The NMVOC
140 speciation also aligns with the MEIC model. This inventory takes priority in integration over MEIC, indicating that only few
141 industrial sources not covered in this inventory are substituted with MEIC.

2.1.3 The YRD air pollutant emission inventory

143 Regional emission inventories in YRD provide a more accurate representation of emissions compared to the national-scale
144 MEIC, as proven by ground and satellite observations (Zhou et al., 2017a; Zhao et al., 2018; Zhao et al., 2020; Zhang et al.,
145 2021; Zhao et al., 2017b; Yang and Zhao, 2019). This improvement is attributed to the avoidance of outdated or non-localized
146 emission calculation parameters, commonly present in large-scale inventories like MEIC. Here, we merge the 2017 YRD air
147 pollutant emission inventory into INTAC for state-of-the-art estimates of rapidly changing emissions over this core area (An
148 et al., 2021; Gu et al., 2023; Zhou et al., 2017a).

149 Localized field surveys and measurements greatly enhance the reliability of calculation parameters within the YRD inventory.

150 Highly-resolved emissions for the power sector are acquired through on-site monitoring with high temporal resolution (Zhang

151 et al., 2019b), rather than relying on static and outdated average emission factors. Facility-level information (e.g., the removal

152 efficiencies) obtained from local investigation and a segment-based industrial process method enhances understanding of both

153 the quantity and spatial patterns of industrial emissions. Considering meteorological factors and land use conditions during

154 agricultural processes results in more accurate seasonal and spatial distributions of NH_3 emissions. (Zhao et al., 2020). An

155 investigation of in-use machinery is conducted to capture the seasonal emission patterns from off-road machines (Zhang et al.,

156 2020). Real-world surveys are performed to determine grain straw ratios and household burning proportions, facilitating the

157 quantification of emissions from biomass-fueled stoves. The $PM_{2.5}$ and NMVOC speciation profiles are updated based on

158 multi-instrument sampling and analysis in both current and previous studies (Huang et al., 2018; Zhao et al., 2017b), satisfying

159 the needs for simulating $PM_{2.5}$ chemical components and O_3. The YRD inventory is collected with a spatial resolution of 0.1

160 degree and an annually temporal resolution in this study. Only CB05 VOC species are collected.

2.1.4 The PRD emission inventory

162 The regional emission inventories in the RPD region demonstrated enhanced reliability compared to previous studies (Huang

163 et al., 2021; Sha et al., 2021; Zheng et al., 2012). The PRD emission inventory in this study captures spatial and temporal

164 variations within the Pearl River Delta region under emission control policies, serving as a foundation for supporting air quality

165 modeling (Huang et al., 2021; Sha et al., 2021).

166 The PRD inventory exhibits notable accuracy improvements, achieved through big data-driven estimation methods, updated

167 spatial-temporal allocations, and localized NMVOC speciation profiles. Gridded hourly open biomass burning emissions are

168 quantified by fusing the fire radiative power data from three satellites, and hourly shipping emissions are estimated using high-

169 frequency AIS records. Thirty-one monthly profiles and ten spatial proxies are updated to reflect spatial-temporal patterns of

170 emissions influenced by economic growth and energy consumption adjustment. Approximately 90% of industrial emissions

171 are disaggregated using exact locations, and novel proxies (e.g., farmland production potential) have been developed for

172 several sectors. The NMVOC speciation is carried out through massive localized measurements and literature reviews,

173 manifested as a collection of 480 NMVOC source profiles across eight sectors and 380 species. The species relevant to the

174 SAPRC-07 chemical mechanism are collected here. Additionally, the inventory encompasses 800 source categories, placing

175 particular emphasis on incorporating new sectors relevant to VOC emissions. Activity rates are improved through extensive

176 field surveys and data mining efforts, involving investigations of production data for 10,000 industrial plants and the gathering

177 of activity-relevant information for 50 million vehicles. Emission factors that reflect local context are obtained or revised based

178 on source measurements and latest research findings. These updates help mitigate uncertainties in emission estimates for the

179 PRD region. The PRD inventory is initially presented at a monthly resolution and a spatial resolution of 0.05 °, with detailed

180 spatial-temporal allocation proxies outlined in Huang et al. (2021).

2.1.5 The open biomass burning emission inventory in China

As a significant source of CO_2, BC, OC and other pollutants, open biomass burning profoundly influences air quality, climate change, and human health (Reisen et al., 2013). A case study in summer 2011 for the YRD region revealed that during a severe haze episode, open biomass burning contributed to 37%, 70%, and 61% of $PM_{2.5}$, OC, and EC emissions, respectively (Cheng et al., 2014). To address the absence of this source in MEIC, we integrate a high-resolution open biomass burning emission inventory from Peking University into INTAC (Song et al., 2009; Huang et al., 2012a; Yin et al., 2019; Liu et al., 2015b). The inventory applies satellite observations to tackle considerable uncertainties tied to provincial statistical data and overcome the coarse resolution found in previous studies (Ni et al., 2015). The estimation of biomass consumption in the inventory is based on the fire radiative energy (FRE) approach, which depends on the energy emitted by fires. This approach helps reduce the biases introduced by burned areas algorithms, especially for small-scale fires. The inventory utilizes the high spatial resolution land cover dataset GlobeLand30 derived from multispectral images to classify biomass fuel types. Eventually, daily emissions from forest, grassland, cropland and shrubland are calculated at a 1-kilometer resolution. The reasonableness is validated by comparing with other datasets, such as the fourth version of the Global Fire Emissions Database. The initially collected inventory lacks VOC model species.

2.1.6 The shipping emission inventory in East Asia

In recent years, maritime trade in the East Asian region has significantly increased (Trade and Development, 2014), resulting in a surge in shipping emissions with substantial impacts on air quality and climate. Previous studies have indicated that East Asian shipping emissions accounted for 16% of the global total in 2013. Shipping emissions made a growing contribution to the rise in annual mean $PM_{2.5}$ concentrations, reaching levels as high as 5.2 μg/m^3 in 2015 (Lv et al., 2018). To address the omission of this emission source in the MEIC, we integrate the shipping emission inventory in East Asian for 2017 into INTAC (Liu et al., 2016b; Liu et al., 2019).

The inventory introduces an innovative approach based on comprehensive and dynamic ship activity data. A static dataset of approximately 66,000 vessels is compiled as a foundation, using information from Lloyd's Register and China Classification Society. This dataset encompasses various ship properties, including ship category, hull shape, engine rotational speed, engine capacity, maximum speed capability, build year, and more. High quality Automatic Identification System (AIS) data is used to capture ship activities, incorporating the Maritime Mobile Service Identification identifier, geographical location, real-time speed, and time-related information. This data is also employed to generate gridded emissions from shipping at a spatial resolution of 0.1 °. The inventory enhances our comprehension of regional-level shipping emissions and significantly alleviates biases arising from the misallocation of marine fuels, as observed in global studies (Endresen et al., 2007). The collected shipping inventory provides emissions at an annually resolution for seven species, including SO_2, NO_x, CO, NMVOC, $PM_{2.5}$, BC, and OC.

212 **2.1.7 PKU-NH₃**

213 As a prominent alkaline component in the atmosphere, ammonia plays a crucial role in atmospheric chemistry, terrestrial and

214 aquatic ecosystems through its participation in atmospheric reactions and deposition processes. This study integrates PKU-

215 NH$_3$, a high-resolution ammonia emission inventory for China developed by Peking University. PKU-NH$_3$ is designed to track

216 the evolution of NH$_3$ emissions amid the rapid increase in grain and meat production in China over the past few decades

217 (Huang et al., 2012b; Kang et al., 2016). This inventory offers a better grasp on NH$_3$ emissions in China through the application

218 of a processed-based method and more reliable emission factors, in contrast to previous studies (Kurokawa et al., 2013; Li et

219 al., 2017b).

220 Earlier studies of NH$_3$ emissions commonly used fixed EFs, overlooked some ammonia emission sources, and had coarse

221 resolutions (Streets et al., 2003; Ohara et al., 2007). Unlike previous approaches, the PKU-NH$_3$ incorporates dynamic and

222 multifactorial EFs and more comprehensive emissions sources. The determination of emission factors takes into account

223 various parameters related to local conditions and agricultural practices. When estimating NH$_3$ emissions of synthetic fertilizer

224 application, the model considers five types of fertilizers, as well as factors such as soil acidity, ambient temperature, fertilizer

225 application technique and dosage, wind speed, and in-situ measurements of NH$_3$ flux. For livestock waste, NH$_3$ emissions are

226 calculated using a mass-flow approach across four phases of manure management, considering variables such as animal rearing

227 types, temperature and wind speed. In addition, NH$_3$ emissions from other small sources are also quantified, including

228 agricultural soil, nitrogen-fixing crop, crop residue compost, excretion of rural populations, open biomass burning, waste

229 disposal, gasoline vehicles, diesel vehicles, and industrial processes. The NH$_3$ emissions are allocated from provinces into 0.1 °

230 grids based on spatial proxies such as land cover, rural population, and other relevant indicators. Monthly emission factors

231 shaped by meteorological conditions are used to calculate NH$_3$ emissions from fertilizer application and livestock source at a

232 monthly level.

233 **2.2 The integration of multi-source heterogeneous data**

234 In the integration process, seven heterogeneous inventories are first normalized in terms of emission sources, species, spatial-

235 temporal resolutions, and then integrated following a priority order to produce a standardized, highly-resolved data cube.

236 **2.2.1 Source mapping**

237 To merge inventories under a unified emission source classification system, the emission sources in the MEIC model are

238 categorized into 88 standard sectors for mapping. The first-level category comprises 8 subcategories, namely, power, industry,

239 residential, transportation, agriculture, solvent use, shipping, and open biomass burning. These are then further subdivided into

240 88 second-level sources, which take industrial classification for national economic activities for reference. For example, the

241 industrial process sector encompasses emission sources such as the manufacturing of non-metallic mineral products,

242 manufacturing of chemical fibers, manufacturing of foods, smelting and pressing of ferrous metals, and more. In the initial

243 step of integration, the sectors from each emission inventory are mapped to the standardized two-level sources.

2.2.2 Species mapping

245 Then, non-methane volatile organic compounds (NMVOC), particulate matter (PM), and NO_x in each inventory are converted

246 into model-ready species to support CTMs. The species mapping process is grounded in the chemical species mapping methods

247 in MEIC model (Li et al., 2017b; Li et al., 2014). The model supports aerosol chemical schemes such as AER05 and AER06.

248 NO_x emissions are allocated to NO and NO_2 emissions based on ground observations. The step-by-step NMVOC speciation

249 framework developed in Li et al. (2014) is employed to generate emissions for various gas-phase chemical mechanisms

250 commonly used in CTMs, including CB-IV, CB05, SAPRC-07, SAPRC-99 and RADM2. The framework incorporates an

251 explicit assignment approach and updated profiles based on both local measurements and the SPECIATE database v.4.5. The

252 sources abundant with oxygenated volatile organic compounds (OVOC) are identified, and the incomplete profiles with

253 missing OVOC fractions are corrected. The accurate speciation mapping helps reduce uncertainties in model-ready emissions.

254 For inventories providing speciated VOC emissions for certain mechanisms (e.g., the YRD inventory for CB05, PRD inventory

255 for SAPRC-07), we directly use their emissions, or alternatively, utilize MEIC's speciation framework to generate model

256 species for the five chemical mechanisms.

2.2.3 Temporal disaggregation

258 The seven emission inventories are collected at different temporal resolutions (Table 1) and need to be temporally allocated to

259 a unified monthly scale for integration. Monthly emissions from PKU-NH₃, the PRD inventory, the industrial point source

260 inventory and MEIC can be directly used for data merge. Daily-level open biomass burning emission inventory for China is

261 aggregated to monthly scales through summation. For annually inventory (e.g., the YRD inventory), sector-specific monthly

262 profiles derived from the MEIC model are used for disaggregation (Li et al., 2017b). For instance, monthly power generation

263 data from the National Bureau of Statistics describe variations in monthly power emissions. Industrial production or GDP from

264 the National Bureau of Statistics are employed to account for monthly emission fluctuations related to industrial heating,

265 boilers, cement, iron and steel, and other industrial processes. Monthly emission factors calculated by the International Vehicle

266 Emissions model are applied to on-road vehicles. Considering the insignificant monthly variations of Automatic Identification

267 System data for marine shipping, the annual shipping emissions are uniformly disaggregated across the months.

2.2.4 Spatial allocation

269 The seven inventories are in different data formats, including point source and gridded formats at varying resolutions,

270 necessitating spatial harmonization for integration. Gridded emissions finer than 0.1 ° resolution are aggregated to 0.1 °, which

271 is performed in the open biomass burning inventory and the PRD inventory. For the industrial point source inventory, latitude

272 and longitude coordinates are employed to directly position them within grid locations. Area sources in MEIC are allocated to

273   grids using spatial proxies within the MEIC model (Li et al., 2017b). For instance, industrial sources are assigned to grids

274   based on urban population (Schneider et al., 2009). The road network (Zheng et al., 2014) serves as a proxy for disaggregating

275   emissions from on-road vehicles, while rural population (Schneider et al., 2009) is used as the proxy for fertilizer and livestock

276   sources. All the emissions are first uniformly downscaled to 1 km, and then re-gridding to 0.1 ° after the spatial-temporal

277   coupling process.

278   **2.2.5 Spatial-temporal coupling**

279   Finally, following the procedures outlined in Sections 2.2.1 to 2.2.4, all inventories are preprocessed to a standardized format,

280   encompassing 88 sectors, various species, a spatial resolution of 1 km, and a monthly temporal resolution. This preprocessing

281   prepares the inventories for merging, ultimately resulting in the generation of a standardized data cube.

282   The integration is carried out at source-by-source, species-by-species, and grid-by-grid levels, with the process guided by the

283   priority order of each inventory (Table 1). MEIC serves as the default inventory in our integration, offering extensive spatial

284   and species coverage, along with spatial proxies, temporal profiles, and NMVOC speciation methods within the model. The

285   remaining six emission inventories are assigned a predefined priority order. The industrial point source emission inventory for

286   China takes precedence over industrial emissions in MEIC, substituting proxy-based spatial allocation with precise

287   geographical coordinates. This extends the applicability of MEIC from a resolution greater than 0.25 ° to the kilometer scale

288   (Zheng et al., 2017; Zheng et al., 2021). To achieve fine-grained emission characterization in critical areas, the YRD and PRD

289   emission inventory enriched with localized data and advanced methods are incorporated to update emissions in these areas.

290   While MEIC comprehensively estimates emissions for ~800 source categories in China, there may still be omissions for certain

291   emission sources. The inclusion of inventories for open biomass burning and East Asian shipping helps partially fill this gap.

292   The PKU-NH_3, generated by a process-based model to provide a comprehensive understanding of China's NH_3 sources, is

293   utilized to replace all NH_3 emissions in other inventories. It's worth noting that the prioritization is performed city by city. For

294   emissions of a particular species from a specific emission sector, when multiple inventories overlap in city grids, the estimates

295   from the highest-priority inventory is selected as the final emissions. Through this step, the integrated inventories are developed

296   based on the configured output settings, such as map projection and spatial-temporal attributes.

297   **2.3 Evaluation of the emission inventory using WRF/CMAQ model**

298   We apply Weather Research and Forecasting Version 3.9 (WRFv3.9) and Community Multiscale Air Quality Version 5.2

299   (CMAQ5.2) as the air quality simulation systems. Two nested simulation domains with horizontal resolutions of 36 and 12

300   km are used (Fig. S1). The mother domain (172 × 127 cells) covers the entire China and parts of the neighboring countries,

301   and the nested domain (226 × 241 cells) includes the heavily polluted Eastern China. Four month (January, April, July, and

302   October) simulation in 2017 is carried out, with a 7-day spin-up period preceded each month. The vertical resolution in WRF

303   is set with 45 sigma levels ranging from the surface up to 100 hPa. Subsequently, it is collapsed into 28 layers through the

304   Meteorology-Chemistry Interface Processor (MCIP) before being input into CMAQ.

305 The configuration of WRF and CMAQ model in this study follows Cheng et al. (2019). The initial and boundary conditions

306 for the simulation are provided by the final reanalysis data from the National Centers for Environmental Prediction (NCEP-

307 FNL, https://rda.ucar.edu/datasets/ds083.2/). The schemes for shortwave radiation, longwave radiation, land surface processes,

308 boundary layer, cumulus parameterization, and cloud microphysics are selected as the New Goddard scheme (Chou et al.,

309 1998), RRTM scheme (Mlawer et al., 1997), Pleim–Xiu surface layer scheme (Xiu and Pleim, 2001), ACM2 PLB scheme

310 (Pleim, 2007), Kain-Fritsch scheme (Kain, 2004), and WSM6 scheme (Hong and Lim, 2006), respectively. Observational

311 nudging and soil nudging are employed to enhance the meteorological simulation. Regarding CMAQ model, the chemical

312 mechanisms for gas-phase, aqueous-phase, and aerosol are configured as CB05, the Regional Acid Deposition Model (RADM),

313 and AERO6, respectively. Photolysis rates are calculated online using the simulated aerosols and ozone concentrations.

314 Anthropogenic emissions outside China are taken from MIX inventory (Li et al., 2017b). The integrated inventory INTAC and

315 MEIC are used for comparison within China. Biogenic emissions are calculated using the Model of Emissions of Gases and

316 Aerosols from Nature version 2.1 (MEGANv2.1), while dust and lightning emissions are not considered in this study.

317 The performances of WRF for the meteorological parameters are evaluated against the Integrated Surface Database (ISD) from

318 the National Climatic Data Center (NCDC) of the National Climate Data Center (ftp://ftp.ncdc.noaa.gov/pub/data/noaa/).

319 Evaluation metrics include correlation coefficient (R), mean bias (MB), root mean square error (RMSE), normalized mean

320 bias (NMB), and normalized mean error (NME). Table S1 demonstrates good agreement between WRF model results and

321 ground-level observations. Similar configurations have been also validated in previous studies (Cheng et al., 2019; Cheng et

322 al., 2021a; Cheng et al., 2021b). CMAQ modeling results are assessed using hourly observed concentrations of air pollutants

323 obtained from the China National Environmental Monitoring Center (http://www.cnemc.cn/).

324 3 Results

325 3.1 China's emission characteristics in 2017

326 We utilized the integrated emission inventory to analyze pollutant emissions in China for the year 2017. Major air pollutant

327 emissions were estimated as follows: 12.3 Tg SO_2, 24.5 Tg NO_x, 141.0 Tg CO, 27.9 Tg NMVOC, 9.2 Tg NH_3, 11.1 Tg PM_{10},

328 8.4 Tg $PM_{2.5}$, 1.3 Tg BC, and 2.2 Tg OC. The emission data for the eight first-level sectors can be downloaded from

329 https://doi.org/10.5281/zenodo.10459198 (Wu et al., 2024). The following sections will characterize emissions in detail across

330 sectors, fuel types, and spatial distributions.

331 3.1.1 By sectors

332 Table 2 displays emissions specific to the eight first-level sectors in the integrated emission inventory INTAC. For pollutants

333 primarily originating from fuel combustion and industrial processes (e.g., SO_2, NO_x, CO, PM_{10}, and $PM_{2.5}$), power, industry,

334 and transportation sources make a significant contribution to their emissions, ranging from 56% to 83%. Industrial sources

335 take a leading role in various atmospheric pollutants, contributing more than 30% for SO_2, NO_x, CO, NMVOC, PM_{10}, and

336 PM$_{2.5}$ emissions. Due to low combustion efficiency and a lack of emission control measures, residential sources exhibit a high

337 emission factor for products of incomplete combustion, leading to 40% of CO emissions, 48% for BC, and 73% for OC.

338 Solvent sources exclusively produce NMVOC emissions, constituting 33% to the overall emissions. The complexity of VOC

339 emission origins is evident in the diverse range of contributing sources. Agricultural sources dominate NH$_3$ emissions,

340 comprising an 83% share of total emissions. As described in Sect. 2.1.7, the PKU-NH$_3$ incorporates a wide variety of NH$_3$

341 sources, providing a more comprehensive understanding of the sectors contributing to NH$_3$ emissions. Insignificant sources

342 may exert large influence in specific regions or periods, such as during large wildfires or in cities with heavy traffic.

343 Additionally, the contribution of the supplemented open biomass burning source cannot be overlooked, especially for OC (7%)

344 and NMVOC (6%).

345 **Table 2: Anthropogenic emissions of air pollutants by sectors in the 2017 INTAC inventory for China (Units: Gg).**

Sectors	SO$_2$	NO$_x$	CO	NMVOC	NH$_3$	PM$_{10}$	PM$_{2.5}$	BC	OC
Power	1822	3790	4909	152	14	981	568	6	0
Industry	6066	8800	52828	8824	249	5603	3620	308	285
Residential	2361	861	55895	3676	629	3516	3088	606	1649
Transportation	341	7751	22597	4123	619	533	493	257	95
Agriculture	0	0	0	0	7609	0	0	0	0
Solvent	0	0	0	9255	0	0	0	0	0
Shipping	1642	3077	391	191	2	73	264	43	49
Open biomass burning	21	215	4403	1659	76	409	355	35	167
Total	12253	24494	141023	27881	9198	11117	8388	1255	2245

346 Figure 2 consolidates 88 standardized emission sources into 25 categories, allowing for a more detailed analysis of sectoral

347 emission patterns compared to Table 2. Owing to substantial coal use in industrial and power sectors, along with sulfur-rich

348 ship fuels, prominent contributors to SO$_2$ emissions include power, shipping, stationary combustion, and manufacture of non-

349 metallic mineral products sources, accounting for 15%, 13%, 12%, and 12% respectively to total SO$_2$ emissions. This indicates

350 that achieving further reductions in SO$_2$ emissions will require the implementation of more energy-efficient, end-of-pipe

351 control measures, and adoption of low-sulfur fuels. The dominant origins of NO$_x$ emissions are from the truck, power

352 generation, and shipping sectors, representing 21%, 15%, and 13% of the total emissions. Both trucks and vessels extensively

353 use compression ignition engines, prone to generating NO$_x$ emissions under high-temperature and oxygen-rich conditions.

354 Implementing strict vehicle standards is crucial to effectively reduce NO$_x$ emissions from exhaust gases. Coatings, other

355 industrial processes, and passenger vehicle sources constitute 51% of anthropogenic NMVOC emissions. The major

13

356 contributors to primary $PM_{2.5}$ emissions include biomass fuel, the manufacture of non-metallic mineral products, and the

357 smelting and pressing of ferrous metals source, making up 22%, 17%, and 10% of the total emissions, respectively. It's

358 noteworthy that the use of biomass fuels (e.g., rice straw, firewood) for cooking or heating in rural areas results in considerable

359 $PM_{2.5}$ emissions, especially in provinces like Sichuan, Anhui, Shandong, and Heilongjiang.
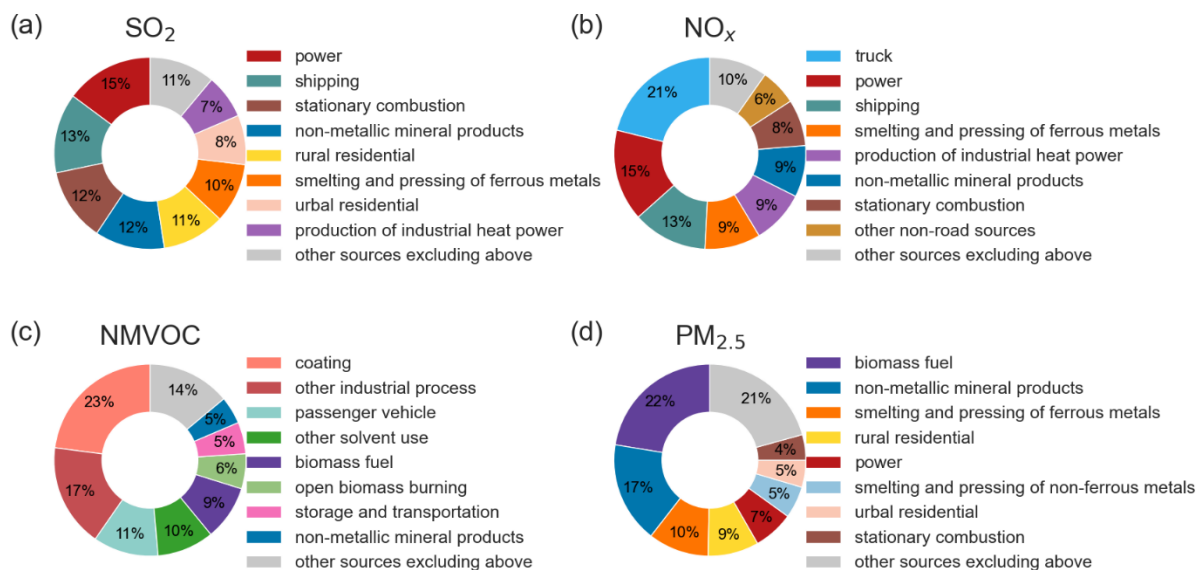
360 **Figure 2: Sector-specific distributions of emissions in the 2017 INTAC inventory for China.** (a), (b), (c) and (d) represent the sectoral
361 contributions for SO_2, NO_x, NMVOC and $PM_{2.5}$, respectively. The figure only displays the top eight contributing sources, while sources
362 excluding these are categorized as "other sources".

363 3.1.2 By fuel types

364 Figure 3 illustrates the proportions of major air pollutant emissions in 2017 for each fuel type. Fossil fuel combustion

365 significantly dominates the emissions of PM_{10}, $PM_{2.5}$, CO, BC, SO_2, NO_x, with proportion ranging from 38% to 80%. The coal

366 combustion accounts for 56% of SO_2 emissions, with power, residential activities and industrial production as the primary

367 emitter. Meanwhile, petroleum combustion, mainly from marine vessels, constitutes 20% of SO_2 emissions. For NO_x emissions,

368 petroleum combustion contributes 48% of the total, predominantly arising from freight trucks (5.2 Tg), marine vessels (3.1

369 Tg), and passenger vehicles (1.0 Tg). Coal combustion processes, such as power (3.6 Tg) and industrial boiler (2.2 Tg) also

370 result in substantial NO_x emissions (31%). The Biomass fuel source causes 53% of OC emissions. Emissions of NMVOC and

371 NH_3 are primarily associated with non-combustion processes.
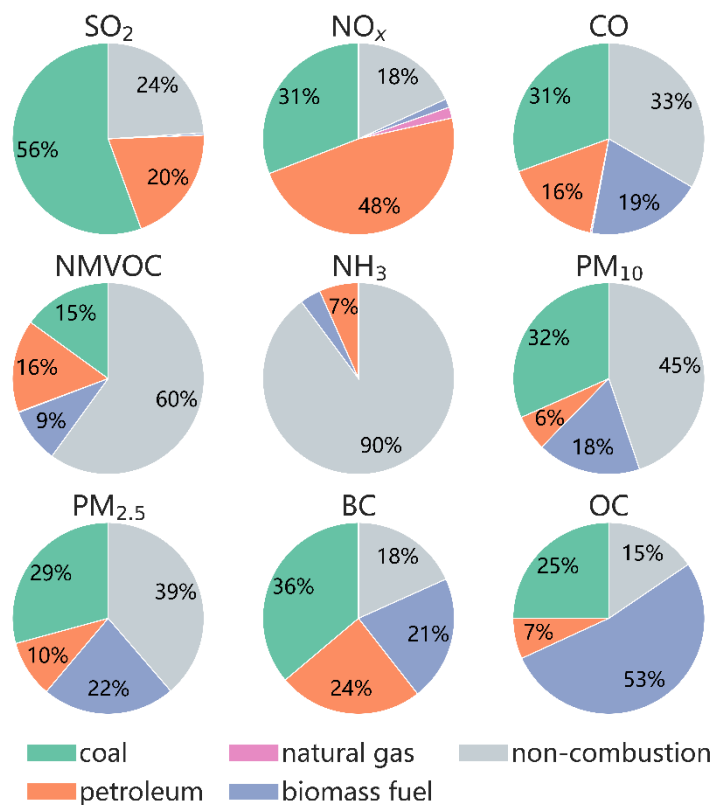
Figure 3: Fuel-specific distributions of major air pollutant emissions in the 2017 INTAC inventory for China.

3.1.3 Spatial distribution

We present the gridded emission maps of major air pollutants in Fig. 4. Emissions from anthropogenic sources in China exhibit significant spatial heterogeneity. Due to economic growth and industrial activities, air pollutant emissions are primarily concentrated in the central and eastern regions of China, especially in economically developed urban clusters such as the Beijing-Tianjin-Hebei region, the YRD, the PRD, as well as in regions like Sichuan and Chongqing. These four key areas account for 26%, 34%, 35%, 37%, 35%, 33%, 27%, 27%, and 29% of the national emissions of SO_2, NO_x, CO, NMVOC, NH_3, PM_{10}, $PM_{2.5}$, BC, and OC, respectively. Moreover, the emission maps at a fine spatial resolution of $0.1°×0.1°$ depict the local variations in emission patterns, identifying numerous hotspots in small areas and showcasing distinct gradients in emissions. Table 3 shows the provincial-level emissions. The emission levels in specific provinces are determined by factors such as resource endowments, industrial structure, energy consumption, and emission control measures. Taking SO_2 as an example, the top five provinces are Shanxi, Shandong, Hebei, Guizhou, and Inner Mongolia, collectively accounting for 36% of the national total SO_2 emissions. The Guizhou Province, located in the southwest of China, is characterized by high-sulfur coal and a relatively gradual implementation of pollution control measures, which results in elevated SO_2 emissions. In other four provinces, large scale heavy industries have led to substantial coal consumption and correspondingly higher SO_2 emissions.

387   Provinces with a less industry-focused economic structure and lower energy consumption, including Tianjin, Hainan, Qinghai,

388   Beijing, and Tibet, exhibit the lowest SO_2 emissions, accounting for approximately 2% of the national total.
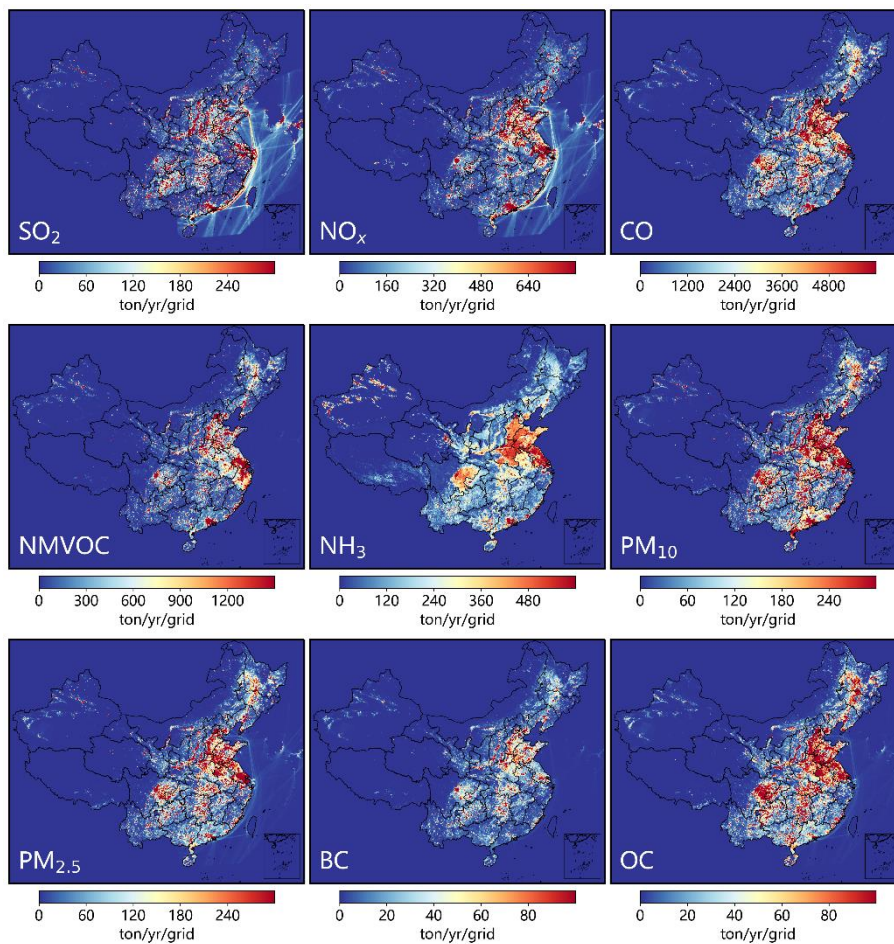
389   **Figure 4: Spatial distributions of major air pollutant emissions in the 2017 INTAC inventory for China.**

Earth System
Science
Data

390 **Table 3: Anthropogenic emissions of air pollutants by provinces in the 2017 INTAC inventory for China (Units: Gg).** The shipping
391 emission inventory in East Asia is not included.

Sectors	SO$_2$	NO$_x$	CO	NMVOC	NH$_3$	PM$_{10}$	PM$_{2.5}$	BC	OC
Anhui	319	850	5968	1094	340	603	447	50	116
Beijing	27	232	1397	519	36	62	50	7	16
Chongqing	401	377	2424	566	149	210	160	22	48
Fujian	162	532	2349	899	149	204	153	22	49
Gansu	191	353	2225	359	276	165	127	22	42
Guangdong	435	1573	6912	1274	351	793	359	17	68
Guangxi	268	436	3586	811	323	359	277	29	84
Guizhou	660	357	6643	510	236	464	350	76	127
Hainan	48	95	586	172	57	47	37	5	15
Hebei	675	1704	11756	1681	522	717	532	88	126
Heilongjiang	249	825	7049	1426	378	501	407	65	158
Henan	371	1262	7979	1507	677	628	463	79	109
Hubei	519	706	6355	1188	357	461	357	68	119
Hunan	524	635	6817	958	329	487	366	77	123
Inner Mongolia	601	1217	5760	834	561	465	343	56	90
Jiangsu	395	1222	8646	1536	497	675	500	50	106
Jiangxi	181	451	3684	649	209	277	197	28	53
Jilin	238	655	3982	851	207	310	240	39	77
Liaoning	464	1205	5848	1322	268	437	328	54	88
Ningxia	228	329	767	179	79	92	63	7	9
Qinghai	44	107	599	130	131	60	45	5	8
Shaanxi	338	551	3789	824	273	297	223	39	69
Shandong	957	2144	11494	2859	694	907	684	105	152
Shanghai	116	471	1133	344	29	106	87	16	6
Shanxi	989	968	6030	759	199	561	419	64	82
Sichuan	384	781	6375	1485	644	468	374	56	143
Tianjin	91	335	1437	575	33	82	62	9	12
Xinjiang	260	610	2645	635	515	220	160	23	32
Xizang	1	52	150	46	149	15	12	2	5
Yunnan	335	437	3831	579	397	305	232	38	76
Zhejiang	297	672	3016	1348	118	274	197	23	22

3.2 Improved accuracy of China's anthropogenic emissions by HEIC

3.2.1 Comparison of emission magnitudes with MEIC across sectors and regions

The INTAC inventory improves the representation of anthropogenic air pollutant emissions by incorporating a large number of industrial point sources, integrating high-resolution regional inventories, and supplementing missing emission sources in MEIC. Remarkable differences between INTAC and MEIC are illustrated in Fig. 5 across regions and sectors. Compared to MEIC, the INTAC inventory shows higher levels of 16.7%, 11.5%, 10.8%, 11.0%, and 9.1% for SO_2, NO_x, PM_{10}, $PM_{2.5}$, and OC, respectively. However, it indicates lower levels of 6.3% and 10.6% for NMVOC and NH_3. CO and BC emissions exhibit good agreement between the two inventories, with differences lower than 3.9%. In comparison to MEIC, the supplementary emission sources in INTAC—specifically, open biomass burning and marine shipping—account for the majority of increased emissions, contributing 95%, 89%, and 74% for SO_2, CO, and $PM_{2.5}$, respectively. Additionally, the incorporation of PKU-NH_3 in INTAC leads to a 21% decrease in NH_3 emissions from agricultural sources, while NH_3 emissions from residential sources and transportation increase by 99% and 13.1 times, respectively. Such difference in agricultural sources is mainly caused by the estimates of synthetic fertilizer (Kang et al., 2016), particularly concerning the treatment of fertilizer types and corresponding emission factors.
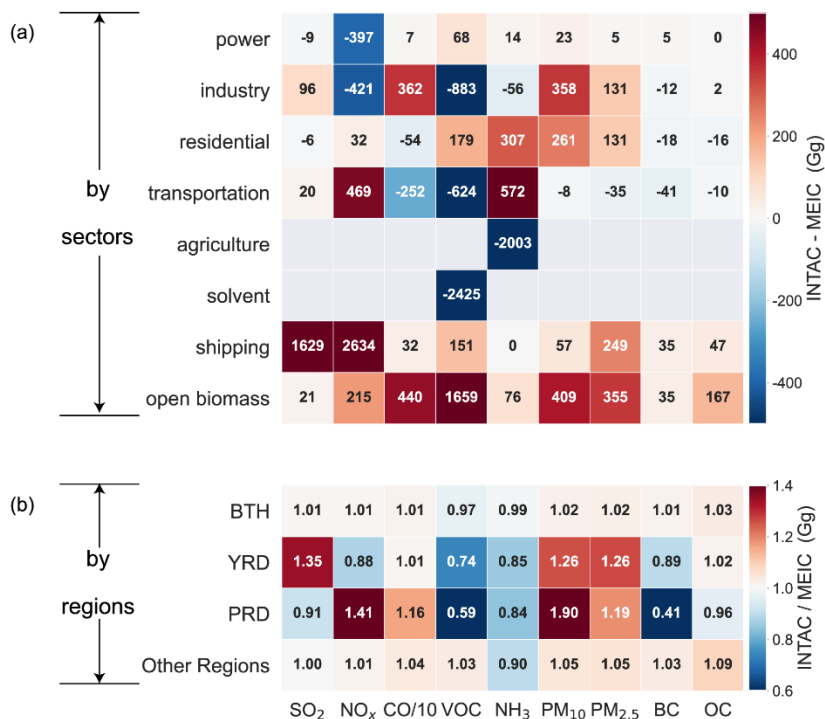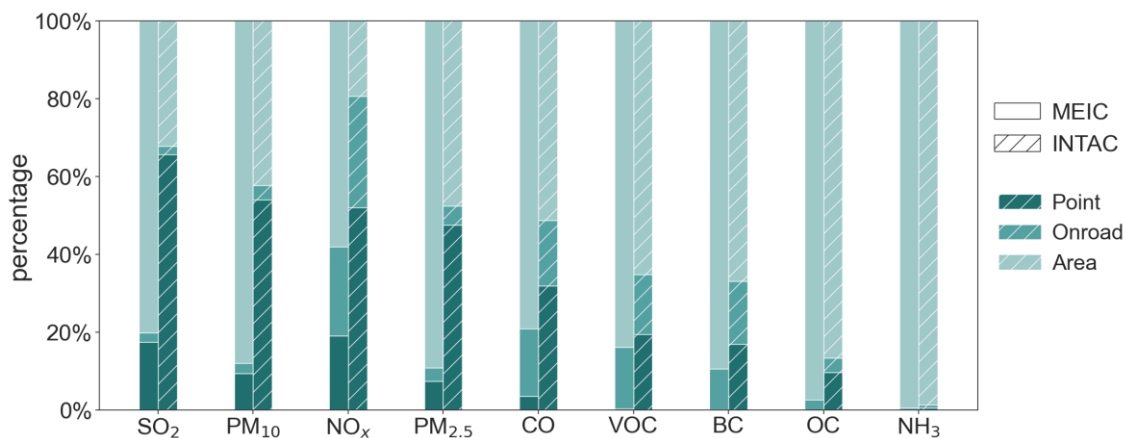

Figure 5: Inter-comparisons of emission estimates between the INTAC inventory and MEIC. (a) shows the difference by sectors, and (b) presents the ratio of emissions in INTAC to those in MEIC. BTH is Beijing-Tianjin-Hebei.

408 Many discrepancies between MEIC and INTAC arise from the integration of regional emission inventories. As presented in
409 Fig. 5b, notable disparities are observed in the YRD and PRD region. Estimates for NO_x emissions in the YRD region are
410 approximately 88% of those derived from the MEIC model. This highlights an enhanced precision attributable to reliable
411 assessments of denitrification efficiency in power plants and the measured NO_x emission factors for both power plants and
412 boilers within the integrated YRD inventory, as supported by previous research studies (Zhao et al., 2018). INTAC's estimates
413 for NMVOC emissions from the YRD region are 26% lower than estimates in MEIC. The overestimation in MEIC mainly
414 results from the uncertainties of solvent use source, particularly coating and printing and dyeing processes. The integrated
415 YRD emission inventory employs more accurate calculation parameters, such as statistical data from local city yearbooks,
416 industry association reports, and apparent consumption of solvents. Furthermore, the speciation profiles of NMVOC are
417 localized and corrected based on the literature research and measurements. In the PRD region, The NO_x emissions from INTAC
418 are 41% higher than MEIC estimates, with non-road sources and non-metallic mineral products contributing 45% and 40% to
419 this difference, respectively. The PRD inventory employs a detailed calculation approach for shipping emissions based on AIS
420 data, in contrast to the simplified approach for inland waterway sources in MEIC. The NO_x emissions from industrial processes
421 of brick and flat glass manufacturing are not considered in MEIC, which is a deficiency that is addressed in the integrated PRD
422 inventory. INTAC's NMVOC emissions are approximately 59% of those from MEIC. The disparity is particularly notable in
423 industrial and solvent use sources, contributing 49% and 35%, respectively, to the observed difference. In INTAC, nearly half
424 of the VOC emission factors for industrial solvent sources are based on local measurements, and a preference for raw material-
425 based calculations over product-based ones reduces uncertainty in the estimation. For significant VOC-emitting sources like
426 cleaning solvents, MEIC employs an emission factor of 1000 g/kg, whereas the PRD inventory uses 850 g/kg. In the case of
427 oil refineries, the emission factors are 2.76 g/kg for MEIC and 1.82 g/kg for the PRD inventory.

428 **3.2.2 Impact of point source contributions**

429 The most accurate method for obtaining emissions at finer-scale grids relies on spatial allocation based on precise geographical
430 coordinates. In MEIC, the majority of emission sources are represented as area sources and distributed onto grids using spatial
431 proxies such as urban population, except for power plants. In contrast, the increased proportion of industrial point source
432 emissions in INTAC significantly constrains the uncertainties associated with spatial proxies. Figure 6 shows the inter-
433 comparisons of percentage of point, on-road, and area source emissions between the INTAC and MEIC. Air pollutants,
434 especially those dominated by industrial combustion sources like SO_2, NO_x, PM_{10}, and $PM_{2.5}$, exhibit a significantly higher
435 proportion of point source emissions within INTAC compared to MEIC. In MEIC, the proportion of point source emissions
436 for SO_2, PM_{10}, NO_x, and $PM_{2.5}$ is 17%, 9%, 19%, and 7%, respectively. However, in the INTAC inventory, these percentages
437 substantially increase to 66%, 54%, 52%, and 48%, respectively, indicating a more accurate representation of spatial patterns.
438 For other species with emissions mainly from area sources, such as residential and transportation, there are limited
439 improvements in the proportion of point source emissions in INTAC.

Figure 6: Inter-comparisons of percentage of point, on-road, and area source emissions between the INTAC inventory and MEIC.

To further assess the impact arising from point sources, Figure 7 takes SO_2 and YRD region as an example to compare the spatial emission patterns between INTAC and MEIC. Figures 7c–e reveal that MEIC tends to overestimate emissions in urban centers and underestimate emissions in rural areas compared to INTAC. The reliance on urban population as a spatial allocation proxy in MEIC becomes unrealistic due to the relocation of factories from city centers amid economic development and rapid urbanization. In Fig. 7f, the grid population is ranked from high to low to analyze the changes in cumulative SO_2 emissions at different spatial resolutions. The findings indicate that when MEIC reaches a 50% cumulative SO_2 emission percentage in densely populated areas at 0.05 ° resolution, INTAC only accounts for 17% of emissions. This highlights that, at a fine grid scale, MEIC allocates more emissions to densely populated urban areas, while INTAC allocates a larger proportion to suburban and rural areas. This reallocation in INTAC aligns better with the actual emission spatial patterns, thereby mitigating biases induced by misallocation based on urban population distributions within MEIC. However, as the grid size gradually increased to 1.0 °, the cumulative emissions in INTAC similarly approach 50%, demonstrating comparable performance to MEIC. This can be attributed to the fact that in larger grid sizes, urban and suburban areas are often encompassed by the same grid, leading to a diminishing spatial accuracy improvement caused by substituting spatial proxies with point sources. Figure 7g further presents the correlation between INTAC emissions and various spatial proxies. At a resolution of 1.0 °, the correlation coefficients between emission distributions and factors (i.e., road networks, nighttime lights, total population, urban population, and rural population) fall within the range of 0.55 to 0.79. Nevertheless, at a resolution of 0.05 °, the correlation coefficients range from 0.05 to 0.13. This indicates that at higher spatial resolutions, INTAC substantially reduces bias introduced by spatial proxies in MEIC.
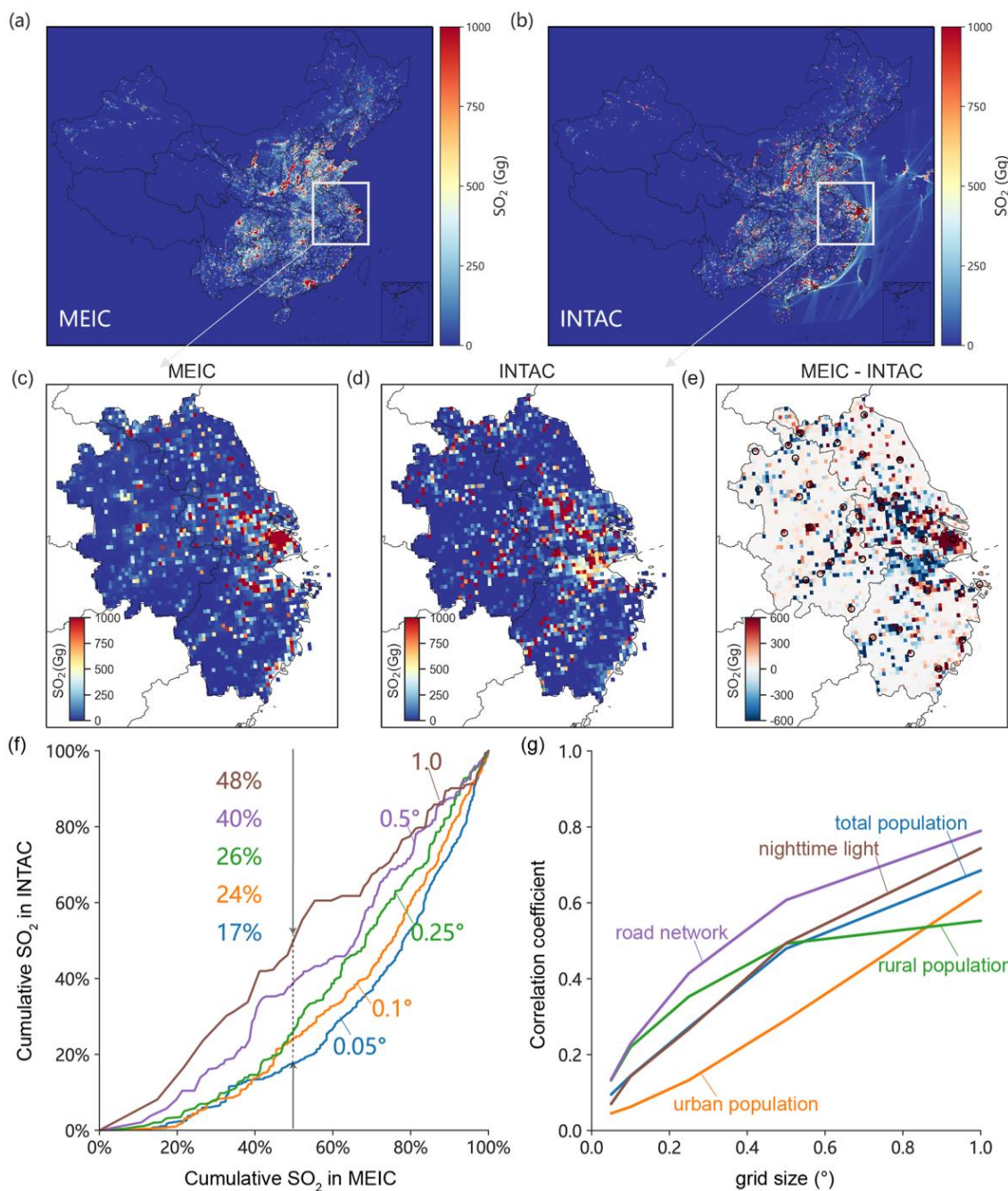
Figure 7: Spatial pattern analysis of emissions in the INTAC inventory, using SO₂ emissions as an example. (a) and (b) display the spatial distributions of SO₂ emissions in MEIC and INTAC, respectively. MEIC emissions have been downscaled from 0.25 degrees to 0.1 degrees for comparison. To compare MEIC and INTAC in details, a zoom-in is applied to the Yangtze River Delta region. (c), (d), and (e) show spatial distributions of SO₂ emissions in MEIC, INTAC and their difference. Circles in (e) represent the center of a city. (f) compares cumulative SO₂ emissions in the INTAC inventory with those in MEIC at different spatial resolutions, with the accumulated calculations performed in descending order of grid population. (g) shows correlation between SO₂ emissions in the INTAC inventory and multiple spatial proxies at different grid sizes.

3.3 Improvements on air quality modelling by HEIC

3.3.1 Overall performance in key regions

We conduct simulations using the WRF-CMAQ model driven by INTAC and MEIC separately to evaluate the improvements in modeled air pollutant concentrations. Table 4 evaluates the simulated emissions in 74 major cities against in-situ observations. The INTAC demonstrates an improved agreement between modeled concentrations and ground-level observations, which benefits from the integrated high resolution inventories. Compared to MEIC, INTAC leads to a decline in the mean bias of simulated major pollutant concentrations by 2–14 μg/m³, a reduction in the root mean square error by 4–19 μg/m³, and a decrease in the normalized mean error by 4–71%. This finding indicates that INTAC produces a more accurate characterization of emissions in China overall. Furthermore, given that atmospheric pollution monitoring stations are mainly located in urban areas in China, the observed differences suggest that the INTAC can mitigate the overestimation of major pollutant concentrations in urban centers. As discussed in Sect. 3.2.2, MEIC overestimates emissions in urban areas and underestimates them in rural and suburban areas, consequently introducing uncertainties into air quality modeling. The enhanced accuracy in spatial distributions in INTAC significantly contributes to enhancing the overall accuracy of concentration modeling.

Table 4: The discrepancies between simulated SO_2, NO_2 and $PM_{2.5}$ concentrations and observed values for 74 major cities at a resolution of 12 km, using MEIC and INTAC as emission inputs. The statistical metrics used for comparison include correlation coefficient (R), mean bias (MB), and root mean square error (RMSE). The bold font represents the difference of modeling performance between INTAC and MEIC.

Pollutants	Inventory	MB (μg/m^3)	RMSE (μg/m^3)	NME (%)
	INTAC	11	30	92
SO_2	MEIC	25	49	163
	Difference	**-14**	**-19**	**-71**
	INTAC	7	22	43
NO_2	MEIC	18	31	60
	Difference	**-11**	**-9**	**-17**
	INTAC	6	35	46
$PM_{2.5}$	MEIC	8	39	50
	Difference	**-2**	**-4**	**-4**

Figure 8 further compares the overall simulation performance between INTAC and MEIC in three key regions (BTH, YRD, and PRD). Regarding $PM_{2.5}$ and its precursors, MEIC shows a considerable mean bias of up to 36 μg/m³ and a root mean square error of up to 59 μg/m³ in key regions. In contrast, INTAC demonstrates values of 15 μg/m³ for MB and 40 μg/m³ for RMSE. The correlation coefficients between simulated and observed concentrations of the three air pollutants are generally

488   lower in MEIC compared to those in INTAC. The modeling performance driven by INTAC, particularly for short-lived

489   pollutants, experiences significant improvement due to their strong correlation with spatial distributions of emission sources.

490   Nonetheless, discrepancies between modeled and observed surface concentrations still exist because of uncertainties from

491   meteorological, physical, and chemical processes within chemical transport models. Moreover, emission sources such as

492   residential, transportation, agriculture in INTAC are treated as nonpoint sources, and their allocation to grids using spatial

493   proxies can introduce biases to air quality modeling. It is noteworthy that simulated ammonium concentrations by INTAC

494   agree better with ground measurements than MEIC (Table S2). While NH_4^+ concentrations are influenced by secondary

495   chemical reactions, the improved model performance still reflects the benefits from the integration of PKU-NH_3.
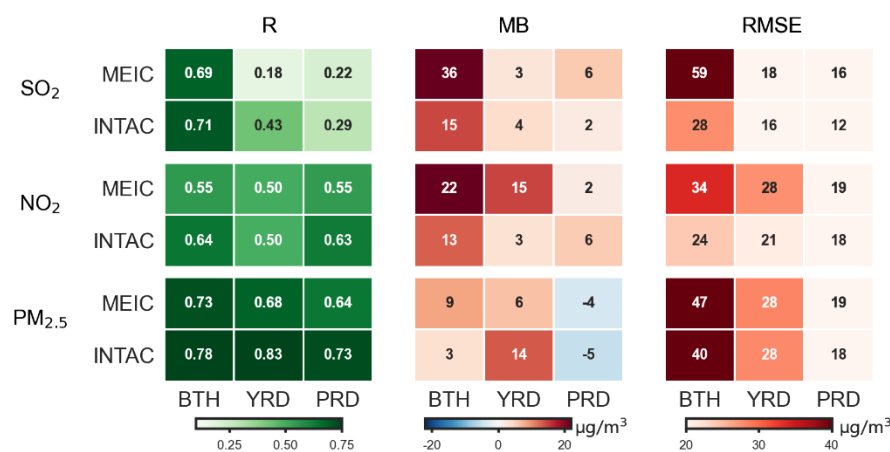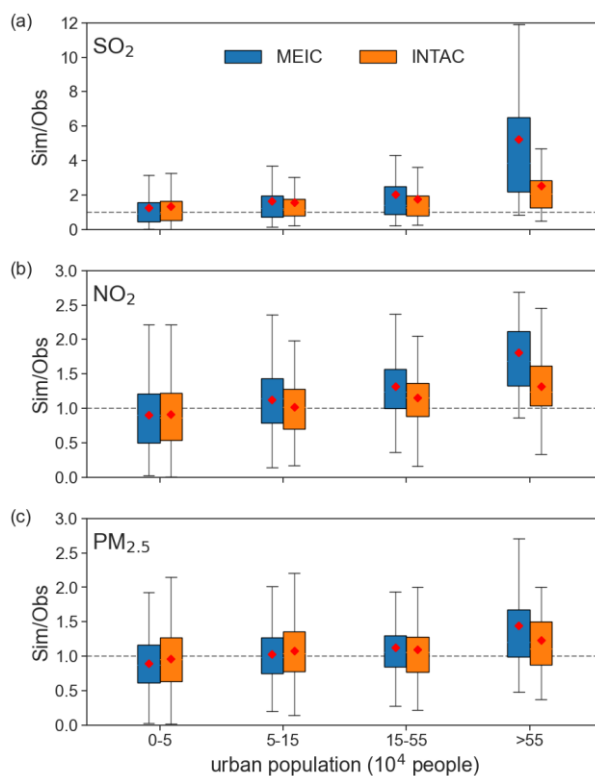

Figure 8: The Comparison of modeling performance across key regions (i.e., BTH, YRD, PRD) when using MEIC and INTAC as emission inputs, respectively. The statistical metrics used for comparison include correlation coefficient (R), mean bias (MB), and root mean square error (RMSE). The regions under comparison comprise the Beijing-Tianjin-Hebei (BTH), Yangtze River Delta (YRD), and Pearl River Delta (PRD).

**3.3.2 Improvements across different spatial resolutions**

501   For a more in-depth assessment for improved spatial patterns in INTAC, Figure 9 categorizes grid cells into different bins

502   based on their urban population and calculates the ratio of simulated pollutant concentrations to ground observations for both

503   INTAC and MEIC in each category. The results demonstrate that as urban population increases, the enhanced model

504   performance of INTAC over MEIC for SO_2, NO_2 and $PM_{2.5}$ becomes more evident. Specifically, when the urban population

505   is less than 50,000, both INTAC and MEIC exhibit a median range of simulated-to-observed concentration ratios close to 1.

506   However, as the urban population exceeds 550,000, the average range for MEIC widens to 1.4–5.2, whereas it remains within

507   the range of 0.9–1.0 for INTAC. This indicates a significant improvement in mitigating the overestimation of emissions in

508   densely populated areas by INTAC. It proves that over-allocated emissions in highly populated areas due to proxy-based

509   methods in MEIC propagate uncertainties into chemical transport models. The incorporation of the industrial point source

510   emission inventory for China, along with the YRD and PRD emission inventory significantly increases point source shares in

511   INTAC, and thus producing better spatial representations of real-world emission distributions and smaller simulated deviations.

512   Discrepancies in model performance between the MEIC and INTAC are influenced by the grid sizes. Figure 10 presents the

513   comparison between modeled SO_2, NO_2 and $PM_{2.5}$ concentrations against ground observations for 74 major cities at resolutions

514   of 36 and 12 km. Increasing spatial resolution can not result in a reduction of simulation errors, particularly for MEIC. As the

515   horizontal resolution increases from 36 km to 12 km, the mean biases of simulated SO_2, NO_2, and $PM_{2.5}$ concentrations using

516   MEIC show an increase from 37% to 143%, 11% to 46%, and -3% to 15%, respectively, when compared to in-situ observations.

517   In contrast, the simulation results using INTAC exhibit better agreement with ground observations, with mean biases for SO_2,

518   NO_2, and $PM_{2.5}$ increasing from 23% to 64%, -0% to 17%, and 2% to 11%, respectively. This is due to the fact that the

519   deviations in finer grid cells, whether overestimated or underestimated, tend to cancel out when aggregated at a coarse spatial

520   resolution. The decoupling between emission spatial distributions with proxies at finer grids leads to more noticeable biases

521   in air quality modeling. Therefore, the findings suggest that the INTAC developed in this study can effectively constrain

522   uncertainties in emissions and the modeling bias, especially at fine spatial scales. The improvement will help tackle emerging

523   challenges in high-resolution air quality modeling in China.

524   **Figure 9: Comparisons of modeling performance between INTAC and MEIC in different ranges of urban population.** The 12 km
525   grids are categorized to different bins according to the urban population residing within each grid. The ratio of simulated pollutant
526   concentrations (Sim) to observed concentrations (Obs) for major pollutants (SO_2, NO_2, and $PM_{2.5}$) are calculated. The boxplot presents the
527   upper quartile, median (red dot), and lower quartile of the ratios.

Earth System
Science
Data

Open Access Discussions
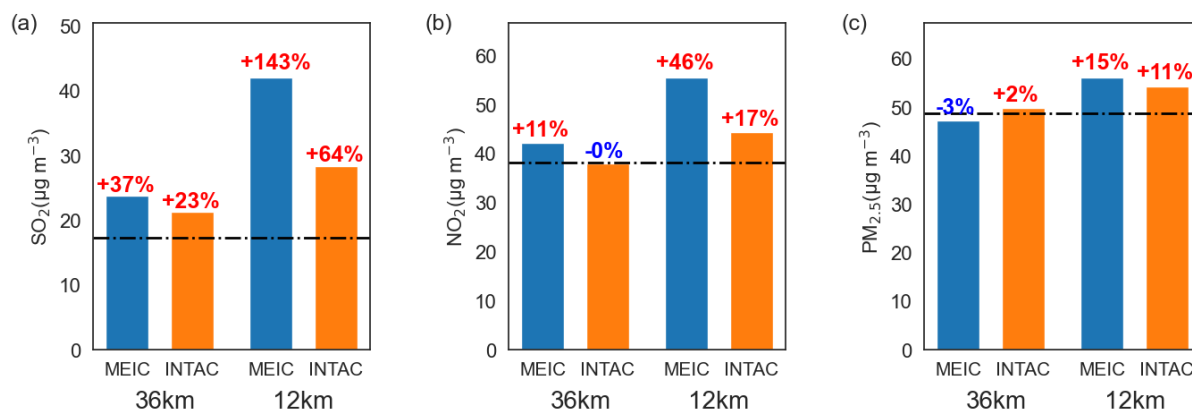
Figure 10: The comparison of modeled air pollutant concentrations and ground observations for 74 cities at 36 and 12 km resolutions, using MEIC and INTAC as emission inputs, respectively. The black dashed line represents the observational mean, and the annotations above the bar charts indicate the mean biases between simulated concentrations and the corresponding observed value.

4 Discussion

Qualitative or quantitative uncertainty assessment is a necessary element of a complete inventory for policy or scientific purposes. Approaches such as error propagation and Monte Carlo simulation are commonly used for quantitative uncertainty analysis in China's emission inventory (Zhao et al., 2017a; Zhao et al., 2011; Lu et al., 2011; Streets et al., 2003). However, this study uses an integrated method rather than a unified framework to compile a comprehensive high resolution emission inventory for China. Collecting only emission quantities from the seven inventories without detailed calculation parameters makes it challenging to assess the overall uncertainties of INTAC here. We have summarized the estimated uncertainty range for components of INTAC in Table 5, where such information is available. Although the uncertainties might be reported for a year other than 2017, they still provide a rough representation of the uncertainty range in major air pollutant emission estimates within INTAC. Species such as SO_2 and NO_x exhibit relatively low uncertainties, benefiting from well-established estimates for large-scale combustion sources. The considerable uncertainties observed in BC and OC emissions may be attributed to inaccuracies in the emission factors of the residential sector. Further details regarding the uncertainties of each component inventory can be found in corresponding literature (Kang et al., 2016; Liu et al., 2016b; Yin et al., 2019; Huang et al., 2021; An et al., 2021; Zhao et al., 2011).

The uncertainties of INTAC also arise from the integrated process: (1) The emission source categories are based on the MEIC model, and sectors in other inventories need to be mapped to the 88 standard sectors first. Due to limited foundational information for an aggregated sector's disaggregation, this process may introduce bias for those who initially provide coarser source categories. For example, YRD only offers one aggregated sector for power, which needs to be broken down into four subsectors (i.e., production of power, supply of power, production of industrial heat power and production of residential heat power). We use the energy consumption for corresponding sectors from the statistical yearbook as a reference basis for this allocation, which is a relatively reliable method despite potential deviations. (2) To generate speciated VOC species, sectoral

552 NMVOC emissions in each inventory need to be matched to corresponding source profiles from the MEIC model.
553 Discrepancies in emission source mapping can impact the outcomes, which will be overcome by gathering more detailed
554 sectoral information for each inventory or directly collecting speciated species in future studies. (3) The INTAC is made
555 publicly available at a monthly scale, given that the majority of its components are gathered on a monthly or annual scale. The
556 temporal disaggregation to finer resolutions for modeling is achieved using empirically selected weighting factors in the MEIC
557 model. However, it is noteworthy that the parameters employed for allocating emissions to daily or hourly scales remain fixed
558 and do not vary over time or region, introducing additional uncertainties. In the future, we plan to incorporate more advanced
559 data or method (e.g., real-time emission measurements) to enhance temporal accuracy at finer scales, as indicated in the
560 previous work for the power sector (Wu et al., 2022). (4) The border issue is inevitable when emissions for the same species
561 in two adjacent cities are derived from different inventories. A typical example is the cities located at the boundary of the YRD
562 or the PRD regions. In the INTAC, we downscale all emissions to 1 km before spatial-temporal coupling process, thereby
563 mitigating this uncertainty to some extent.

564 **Table 5: Uncertainties in the inventory components of INTAC, contingent upon the availability of such information (Unit: %).**

Emission inventory	Reporting year	SO$_2$	NO$_x$	CO	NMVOC	NH$_3$	PM$_{10}$	PM$_{2.5}$	BC	OC	References
PKU-NH$_3$	2012					-26–25					(Kang et al., 2016)
The shipping emission inventory for East Asia	2013	±4	±4	±5	±4			±4	±4	±4	(Liu et al., 2016b)
The open biomass burning emission inventory for China	2003–2017	-67–67	-78–98	-54–56		-44–89	-74–84	-65–65	-75–100	-74–81	(Yin et al., 2019)
The PRD emission inventory	2017	-17–20	-25–28	-30–39	-34–50	-50–86	-45–60	-43–62	-53–116	-54–160	(Huang et al., 2021)
The YRD air pollutant emission inventory	2017	-29–36	-28–33	-42–75	-44–68	-58–117	-36–62	-30–46			(An et al., 2021)
	2005	-14–13	-13–37				-14–45	-17–54	-25–136	-40–121	(Zhao et al., 2011)

565 The INTAC for 2017 is subject to some limitations: (1) The integrated method yields emissions data across various sectors
566 from different datasets for the same city and species, or emissions in different species from different datasets for the same city
567 and sector. The utilization of species ratios requires careful consideration in these cases. (2) Limited resources present a

26

568   substantial challenge in gathering emission inventories over extended time series from diverse research institutions within the

569   scope of this study. The shipping inventory, YRD inventory, and PRD inventory are only accessible for 2017. Consequently,

570   we exclusively present the INTAC for the year 2017, with the possibility of extension to other years in subsequent research.

5 Data Availability

572   Data described in this manuscript can be accessed at Zenodo under https://doi.org/10.5281/zenodo.10459198 (Wu et al., 2024).

6 Concluding remarks

574   Compiling a comprehensive bottom-up emission inventory for China that encompasses both extensive coverage and high

575   resolution poses a formidable challenge. In this work, we construct a 0.1 °resolution integrated inventory for 2017 through the

576   fusion of multi-source emission inventories. An integration model has been developed to couple heterogeneous emission

577   datasets, aimed at generating a standardized data cube with consistent sectors, species and spatial-temporal resolution. The

578   model effectively achieves the generation of a high-resolution, large-scale emission product through source mapping, species

579   mapping, temporal disaggregation, spatial allocation and spatial-temporal coupling. Six representative emission inventories

580   focusing on national and regional scales, as well as key species and sources in China are merged with MEIC, including a point-

581   source-based industrial inventory, two localized inventories for critical regions, two supplementary inventories covering

582   sources omitted in MEIC, and an NH_3 emission inventory. This integration capitalizes on the strengths of each inventory,

583   resulting in an improved depiction of emission totals and spatial distribution patterns for China.

584   We find that the integrated inventory provides a more comprehensive depiction of China's anthropogenic emissions. The total

585   emissions of SO_2, NO_x, CO, NMVOC, NH_3, PM_{10}, $PM_{2.5}$, BC, and OC in 2017 are 12.3, 24.5, 141.0, 27.9, 9.2, 11.1, 8.4, 1.3

586   and 2.2 Tg, respectively. Industrial production serves as the main source of various atmospheric pollutants like SO_2, NO_x, CO,

587   PM_{10}, and $PM_{2.5}$. Residential sources contribute over 40% to CO, BC and OC emissions. Apart from agricultural sources,

588   which account for 83% of NH_3 emissions, it is crucial to acknowledge the contributions from various minor emission sources.

589   This study emphasizes the significance of shipping emissions, particularly in contributing to SO_2 (13%) and NO_x (13%). Fossil

590   fuel combustion dominates the emissions of PM_{10}, $PM_{2.5}$, CO, BC, SO_2, and NO_x, ranging from 38% to 80%. Compared to

591   MEIC, INTAC has greatly improved emission estimates in China. For instance, by integrating the YRD inventory, more

592   accurate quantification of NO_x emission factors and denitrification efficiency results in a 12% reduction in NO_x emissions in

593   INTAC. The incorporation of numerous point sources in INTAC has notably addressed MEIC's tendency to overestimate

594   emissions in urban centers, particularly at higher spatial resolutions. The reduction in emission biases leads to a decrease of

595   uncertainties propagated into the CTMs. In comparison to MEIC, INTAC has exhibited a mean bias reduction in simulated

596   concentrations of major pollutants against ground observations across 74 cities, ranging from 2–14 μg/m³. The improvement

597   in model performance achieved by INTAC is particularly noticeable at finer spatial resolutions.

598 Our study offers an efficient framework for creating highly-resolved emission inventory on a large scale. This framework
599 integrates advantages from previous studies conducted by multiple research organizations and holds the potential to aid
600 policymakers in making well-informed decisions for improving air quality. In the future, we expect the incorporation of a
601 growing number of emission datasets to offer a more reliable representation of emissions in China.

602 **Supplement**

603 The supplement related to this article has one figure (i.e., Figure S1) and two table (i.e., Table S1, S2).

604 **Author contributions**

605 Nana Wu, Guannan Geng, and Qiang Zhang designed the study. Nana Wu developed the INTAC emission inventory and
606 conducted chemical transport modeling. Junyu Zheng, Yu Song, Huan Liu, Yu Zhao, Ying Zhou and Qinren Shi provided the
607 emission inventories for the integration. Ruochong Xu helped with the data analysis. Shigan Liu compiled the chemical
608 transport model. Xiaodong Liu contributed to the design of computer programmes for the integration model. The manuscript
609 was written by Nana Wu and Guannan Geng, and it was revised and discussed by all coauthors.

610 **Competing interests**

611 The authors declare that they have no conflict of interest.

617 **References**

618 An, J., Huang, Y., Huang, C., Wang, X., Yan, R., Wang, Q., Wang, H., Jing, S., Zhang, Y., Liu, Y., Chen, Y., Xu, C., Qiao, L., Zhou, M.,
619 Zhu, S., Hu, Q., Lu, J., and Chen, C.: Emission inventory of air pollutants and chemical speciation for specific anthropogenic sources based
620 on local measurements in the Yangtze River Delta region, China, Atmos. Chem. Phys., 21, 2003-2025, 10.5194/acp-21-2003-2021, 2021.
621 Bo, X., Jia, M., Xue, X., Tang, L., Mi, Z., Wang, S., Cui, W., Chang, X., Ruan, J., Dong, G., Zhou, B., and Davis, S. J.: Effect of strengthened
622 standards on Chinese ironmaking and steelmaking emissions, Nature Sustainability, 4, 811-820, 10.1038/s41893-021-00736-0, 2021.
623 Chen, H., Huang, Y., Shen, H., Chen, Y., Ru, M., Chen, Y., Lin, N., Su, S., Zhuo, S., Zhong, Q., Wang, X., Liu, J., Li, B., and Tao, S.:
624 Modeling temporal variations in global residential energy consumption and pollutant emissions, Applied Energy, 184, 820-829,
625 https://doi.org/10.1016/j.apenergy.2015.10.185, 2016.

Cheng, J., Tong, D., Liu, Y., Bo, Y., Zheng, B., Geng, G., He, K., and Zhang, Q.: Air quality and health benefits of China's current and upcoming clean air policies, Faraday Discussions, 226, 584-606, 10.1039/D0FD00090F, 2021a.

Cheng, J., Tong, D., Liu, Y., Yu, S., Yan, L., Zheng, B., Geng, G., He, K., and Zhang, Q.: Comparison of Current and Future PM2.5 Air Quality in China Under CMIP6 and DPEC Emission Scenarios, Geophysical Research Letters, 48, e2021GL093197, https://doi.org/10.1029/2021GL093197, 2021b.

Cheng, J., Su, J., Cui, T., Li, X., Dong, X., Sun, F., Yang, Y., Tong, D., Zheng, Y., Li, Y., Li, J., Zhang, Q., and He, K.: Dominant role of emission reduction in PM2.5 air quality improvement in Beijing during 2013–2017: a model-based decomposition analysis, Atmos. Chem. Phys., 19, 6125-6146, 10.5194/acp-19-6125-2019, 2019.

Cheng, Z., Wang, S., Fu, X., Watson, J. G., Jiang, J., Fu, Q., Chen, C., Xu, B., Yu, J., Chow, J. C., and Hao, J.: Impact of biomass burning on haze pollution in the Yangtze River delta, China: a case study in summer 2011, Atmos. Chem. Phys., 14, 4573-4585, 10.5194/acp-14-4573-2014, 2014.

Chou, M.-D., Suarez, M. J., Ho, C.-H., Yan, M. M. H., and Lee, K.-T.: Parameterizations for Cloud Overlapping and Shortwave Single-Scattering Properties for Use in General Circulation and Cloud Ensemble Models, Journal of Climate, 11, 202-214, 10.1175/1520-0442(1998)011<0202:PFCOAS>2.0.CO;2, 1998.

Crippa, M., Guizzardi, D., Butler, T., Keating, T., Wu, R., Kaminski, J., Kuenen, J., Kurokawa, J., Chatani, S., Morikawa, T., Pouliot, G., Racine, J., Moran, M. D., Klimont, Z., Manseau, P. M., Mashayekhi, R., Henderson, B. H., Smith, S. J., Suchyta, H., Muntean, M., Solazzo, E., Banja, M., Schaaf, E., Pagani, F., Woo, J. H., Kim, J., Monforti-Ferrario, F., Pisoni, E., Zhang, J., Niemi, D., Sassi, M., Ansari, T., and Foley, K.: The HTAP_v3 emission mosaic: merging regional and global monthly emissions (2000–2018) to support air quality modelling and policies, Earth Syst. Sci. Data, 15, 2667-2694, 10.5194/essd-15-2667-2023, 2023.

Deng, F., Lv, Z., Qi, L., Wang, X., Shi, M., and Liu, H.: A big data approach to improving the vehicle emission inventory in China, Nature Communications, 11, 2801, 10.1038/s41467-020-16579-w, 2020.

Endresen, Ø., Sørgård, E., Behrens, H. L., Brett, P. O., and Isaksen, I. S. A.: A historical reconstruction of ships' fuel consumption and emissions, Journal of Geophysical Research: Atmospheres, 112, https://doi.org/10.1029/2006JD007630, 2007.

Geng, G., Zhang, Q., Martin, R. V., Lin, J., Huo, H., Zheng, B., Wang, S., and He, K.: Impact of spatial proxies on the representation of bottom-up emission inventories: A satellite-based analysis, Atmospheric Chemistry and Physics, 17, 4131-4145, 2017.

Geng, G., Zheng, Y., Zhang, Q., Xue, T., Zhao, H., Tong, D., Zheng, B., Li, M., Liu, F., Hong, C., He, K., and Davis, S. J.: Drivers of PM2.5 air pollution deaths in China 2002–2017, Nature Geoscience, 10.1038/s41561-021-00792-3, 2021.

Gu, C., Zhang, L., Xu, Z., Xia, S., Wang, Y., Li, L., Wang, Z., Zhao, Q., Wang, H., and Zhao, Y.: High-resolution regional emission inventory contributes to the evaluation of policy effectiveness: a case study in Jiangsu Province, China, Atmos. Chem. Phys., 23, 4247-4269, 10.5194/acp-23-4247-2023, 2023.

Hong, S. Y. and Lim, J.-O. J.: The WRF Single-Moment 6-Class Microphysics Scheme (WSM6), Asia-pacific Journal of Atmospheric Sciences, 42, 129-151, 2006.

Huang, C., Hu, Q., Wang, H., Qiao, L., Jing, S. a., Wang, H., Zhou, M., Zhu, S., Ma, Y., Lou, S., Li, L., Tao, S., Li, Y., and Lou, D.: Emission factors of particulate and gaseous compounds from a large cargo vessel operated under real-world conditions, Environmental Pollution, 242, 667-674, https://doi.org/10.1016/j.envpol.2018.07.036, 2018.

Huang, X., Li, M., Li, J., and Song, Y.: A high-resolution emission inventory of crop burning in fields in China based on MODIS Thermal Anomalies/Fire products, Atmospheric Environment, 50, 9-15, https://doi.org/10.1016/j.atmosenv.2012.01.017, 2012a.

Huang, X., Song, Y., Li, M., Li, J., Huo, Q., Cai, X., Zhu, T., Hu, M., and Zhang, H.: A high-resolution ammonia emission inventory in China, Global Biogeochemical Cycles, 26, GB1030, 2012b.

Huang, Z., Zhong, Z., Sha, Q., Xu, Y., Zhang, Z., Wu, L., Wang, Y., Zhang, L., Cui, X., Tang, M., Shi, B., Zheng, C., Li, Z., Hu, M., Bi, L., Zheng, J., and Yan, M.: An updated model-ready emission inventory for Guangdong Province by incorporating big data and mapping onto multiple chemical mechanisms, Science of The Total Environment, 769, 144535, https://doi.org/10.1016/j.scitotenv.2020.144535, 2021.

Janssens-Maenhout, G., Crippa, M., Guizzardi, D., Dentener, F., Muntean, M., Pouliot, G., Keating, T., Zhang, Q., Kurokawa, J., Wankmüller, R., Denier van der Gon, H., Kuenen, J. J. P., Klimont, Z., Frost, G., Darras, S., Koffi, B., and Li, M.: HTAP_v2.2: a mosaic of regional and global emission grid maps for 2008 and 2010 to study hemispheric transport of air pollution, Atmos. Chem. Phys., 15, 11411-11432, 10.5194/acp-15-11411-2015, 2015.

Kain, J. S.: The Kain–Fritsch Convective Parameterization: An Update, Journal of Applied Meteorology, 43, 170-181, 10.1175/1520-0450(2004)043<0170:TKCPAU>2.0.CO;2, 2004.

Kang, Y., Liu, M., Song, Y., Huang, X., Yao, H., Cai, X., Zhang, H., Kang, L., Liu, X., Yan, X., He, H., Zhang, Q., Shao, M., and Zhu, T.: High-resolution ammonia emissions inventories in China from 1980 to 2012, Atmos. Chem. Phys., 16, 2043-2058, 10.5194/acp-16-2043-2016, 2016.

Kurokawa, J., Ohara, T., Morikawa, T., Hanayama, S., Janssens-Maenhout, G., Fukui, T., Kawashima, K., and Akimoto, H.: Emissions of air pollutants and greenhouse gases over Asian regions during 2000–2008: Regional Emission inventory in ASia (REAS) version 2, Atmospheric Chemistry and Physics,13,21(2013-11-13), 13, 2013.

Li, B., Chen, L., Shen, W., Jin, J., Wang, T., Wang, P., Yang, Y., and Liao, H.: Improved gridded ammonia emission inventory in China, Atmos. Chem. Phys., 21, 15883-15900, 10.5194/acp-21-15883-2021, 2021.

682 Li, M., Liu, H., Geng, G., Hong, C., Liu, F., Song, Y., Tong, D., Zheng, B., Cui, H., Man, H., Zhang, Q., and He, K.: Anthropogenic emission
683 inventories in China: a review, National Science Review, 4, 834-866, 10.1093/nsr/nwx150, 2017a.
684 Li, M., Kurokawa, J., Zhang, Q., Woo, J. H., Morikawa, T., Chatani, S., Lu, Z., Song, Y., Geng, G., Hu, H., Kim, J., Cooper, O. R., and
685 McDonald, B. C.: MIXv2: a long-term mosaic emission inventory for Asia (2010-2017), EGUsphere, 2023, 1-45, 10.5194/egusphere-2023-
686 2283, 2023a.
687 Li, M., Zhang, Q., Streets, D. G., He, K. B., Cheng, Y. F., Emmons, L. K., Huo, H., Kang, S. C., Lu, Z., Shao, M., Su, H., Yu, X., and Zhang,
688 Y.: Mapping Asian anthropogenic emissions of non-methane volatile organic compounds to multiple chemical mechanisms, Atmos. Chem.
689 Phys., 14, 5617-5638, 10.5194/acp-14-5617-2014, 2014.
690 Li, M., Zhang, Q., Kurokawa, J. I., Woo, J. H., He, K., Lu, Z., Ohara, T., Song, Y., Streets, D. G., Carmichael, G. R., Cheng, Y., Hong, C.,
691 Huo, H., Jiang, X., Kang, S., Liu, F., Su, H., and Zheng, B.: MIX: a mosaic Asian anthropogenic emission inventory under the international
692 collaboration framework of the MICS-Asia and HTAP, Atmos. Chem. Phys., 17, 935-963, 10.5194/acp-17-935-2017, 2017b.
693 Li, S., Wang, S., Wu, Q., Zhang, Y., Ouyang, D., Zheng, H., Han, L., Qiu, X., Wen, Y., Liu, M., Jiang, Y., Yin, D., Liu, K., Zhao, B., Zhang,
694 S., Wu, Y., and Hao, J.: Emission trends of air pollutants and CO2 in China from 2005 to 2021, Earth Syst. Sci. Data, 15, 2279-2294,
695 10.5194/essd-15-2279-2023, 2023b.
696 Liu, F., Beirle, S., Zhang, Q., Dörner, S., He, K., and Wagner, T.: NOx lifetimes and emissions of cities and power plants in polluted
697 background estimated by satellite observations, Atmos. Chem. Phys., 16, 5283-5298, 10.5194/acp-16-5283-2016, 2016a.
698 Liu, F., Zhang, Q., Tong, D., Zheng, B., Li, M., Huo, H., and He, K. B.: High-resolution inventory of technologies, activities, and emissions
699 of coal-fired power plants in China from 1990 to 2010, Atmos. Chem. Phys., 15, 13299-13317, 10.5194/acp-15-13299-2015, 2015a.
700 Liu, H., Fu, M., Jin, X., Shang, Y., Shindell, D., Faluvegi, G., Shindell, C., and He, K.: Health and climate impacts of ocean-going vessels
701 in East Asia, Nature Climate Change, 6, 1037-1041, 10.1038/nclimate3083, 2016b.
702 Liu, H., Meng, Z.-H., Lv, Z.-F., Wang, X.-T., Deng, F.-Y., Liu, Y., Zhang, Y.-N., Shi, M.-S., Zhang, Q., and He, K.-B.: Emissions and
703 health impacts from global shipping embodied in US–China bilateral trade, Nature Sustainability, 2, 1027-1033, 10.1038/s41893-019-0414-
704 z, 2019.
705 Liu, H., Wu, B., Liu, S., Shao, P., Liu, X., Zhu, C., Wang, Y., Wu, Y., Xue, Y., Gao, J., Hao, Y., and Tian, H.: A regional high-resolution
706 emission inventory of primary air pollutants in 2012 for Beijing and the surrounding five provinces of North China, Atmospheric
707 Environment, 181, 20-33, https://doi.org/10.1016/j.atmosenv.2018.03.013, 2018.
708 Liu, J., Zheng, Y., Geng, G., Hong, C., Li, M., Li, X., Liu, F., Tong, D., Wu, R., Zheng, B., He, K., and Zhang, Q.: Decadal changes in
709 anthropogenic source contribution of PM2.5 pollution and related health impacts in China, 1990–2015, Atmos. Chem. Phys., 20, 7783-7799,
710 10.5194/acp-20-7783-2020, 2020.
711 Liu, M., Song, Y., Yao, H., Kang, Y., Li, M., Huang, X., and Hu, M.: Estimating emissions from agricultural fires in the North China Plain
712 based on MODIS fire radiative power, Atmospheric Environment, 112, 326-334, https://doi.org/10.1016/j.atmosenv.2015.04.058, 2015b.
713 Lu, Z., Zhang, Q., and Streets, D. G.: Sulfur dioxide and primary carbonaceous aerosol emissions in China and India, 1996–2010, Atmos.
714 Chem. Phys., 11, 9839-9864, 10.5194/acp-11-9839-2011, 2011.
715 Lv, Z., Liu, H., Ying, Q., Fu, M., Meng, Z., Wang, Y., Wei, W., Gong, H., and He, K.: Impacts of shipping emissions on PM2.5 pollution
716 in China, Atmos. Chem. Phys., 18, 15811-15824, 10.5194/acp-18-15811-2018, 2018.
717 Mlawer, E. J., Taubman, S. J., Brown, P. D., Iacono, M. J., and Clough, S. A.: Radiative transfer for inhomogeneous atmospheres: RRTM,
718 a validated correlated-k model for the longwave, Journal of Geophysical Research: Atmospheres, 102, 16663-16682,
719 https://doi.org/10.1029/97JD00237, 1997.
720 Ni, H., Han, Y., Cao, J., Chen, L. W. A., Tian, J., Wang, X., Chow, J. C., Watson, J. G., Wang, Q., Wang, P., Li, H., and Huang, R.-J.:
721 Emission characteristics of carbonaceous particles and trace gases from open burning of crop residues in China, Atmospheric Environment,
722 123, 399-406, https://doi.org/10.1016/j.atmosenv.2015.05.007, 2015.
723 Ohara, T., Akimoto, H., Kurokawa, J., Horii, N., Yamaji, K., Yan, X., and Hayasaka, T.: An Asian emission inventory of anthropogenic
724 emission sources for the period 1980–2020, Atmos. Chem. Phys., 7, 4419-4444, 10.5194/acp-7-4419-2007, 2007.
725 Peng, L., Zhang, Q., Yao, Z., Mauzerall, D. L., Kang, S., Du, Z., Zheng, Y., Xue, T., and He, K.: Underreported coal in statistics: A survey-
726 based solid fuel consumption and emission inventory for the rural residential sector in China, Applied Energy, 235, 1169-1182,
727 https://doi.org/10.1016/j.apenergy.2018.11.043, 2019.
728 Pleim, J. E.: A Combined Local and Nonlocal Closure Model for the Atmospheric Boundary Layer. Part I: Model Description and Testing,
729 Journal of Applied Meteorology and Climatology, 46, 1383-1395, 10.1175/JAM2539.1, 2007.
730 Reisen, F., Meyer, C. P., and Keywood, M. D.: Impact of biomass burning sources on seasonal aerosol air quality, Atmospheric Environment,
731 67, 437-447, https://doi.org/10.1016/j.atmosenv.2012.11.004, 2013.
732 Schneider, A., Friedl, M. A., and Potere, D.: A new map of global urban extent from MODIS satellite data, Environmental Research Letters,
733 4, 044003, 10.1088/1748-9326/4/4/044003, 2009.
734 Sha, Q., Zhu, M., Huang, H., Wang, Y., Huang, Z., Zhang, X., Tang, M., Lu, M., Chen, C., Shi, B., Chen, Z., Wu, L., Zhong, Z., Li, C., Xu,
735 Y., Yu, F., Jia, G., Liao, S., Cui, X., Liu, J., and Zheng, J.: A newly integrated dataset of volatile organic compounds (VOCs) source profiles
736 and implications for the future development of VOCs profiles in China, Sci Total Environ, 793, 148348, 10.1016/j.scitotenv.2021.148348,
737 2021.

738   Song, Y., Liu, B., Miao, W., Chang, D., and Zhang, Y.: Spatiotemporal variation in nonagricultural open fire emissions in China from 2000
739   to 2007, Global Biogeochemical Cycles, 23, GB2008, https://doi.org/10.1029/2008GB003344, 2009.
740   Streets, D. G., Bond, T. C., Carmichael, G. R., Fernandes, S. D., Fu, Q., He, D., Klimont, Z., Nelson, S. M., Tsai, N. Y., Wang, M. Q., Woo,
741   J. H., and Yarber, K. F.: An inventory of gaseous and primary aerosol emissions in Asia in the year 2000, Journal of Geophysical Research:
742   Atmospheres, 108, https://doi.org/10.1029/2002JD003093, 2003.
743   Tang, L., Jia, M., Yang, J., Li, L., Bo, X., and Mi, Z.: Chinese industrial air pollution emissions based on the continuous emission monitoring
744   systems network, Scientific Data, 10, 153, 10.1038/s41597-023-02054-w, 2023.
745   Trade, U. N. C. o. and Development: Review of Maritime Transport 2014, United Nations, https://doi.org/10.18356/5a566ab1-en, 2014.
746   Wang, W., Khanna, N., Lin, J., and Liu, X.: Black carbon emissions and reduction potential in China: 2015-2050, Journal of environmental
747   management, 329, 117087, 10.1016/j.jenvman.2022.117087, 2023.
748   Wang, X., Lei, Y., Yan, L., Liu, T., Zhang, Q., and He, K.: A unit-based emission inventory of SO2, NOx and PM for the Chinese iron and
749   steel industry from 2010 to 2015, Science of The Total Environment, 676, 18-30, https://doi.org/10.1016/j.scitotenv.2019.04.241, 2019.
750   Wu, N., Geng, G., Qin, X., Tong, D., Zheng, Y., Lei, Y., and Zhang, Q.: Daily Emission Patterns of Coal-Fired Power Plants in China Based
751   on Multisource Data Fusion, ACS Environmental Au, 2, 363-372, 10.1021/acsenvironau.2c00014, 2022.
752   Wu, N., Geng, G., Yan, L., Bi, J., Li, Y., Tong, D., Zheng, B., and Zhang, Q.: Improved spatial representation of a highly resolved emission
753   inventory in China: evidence from TROPOMI measurements, Environmental Research Letters, 16, 084056, 10.1088/1748-9326/ac175f,
754   2021.
755   Wu, N., Geng, G., Xu, R., Liu, S., Liu, X., Shi, Q., Zhou, Y., Zhao, Y., Liu, H., Song, Y., Zheng, J., and Zhang, Q.: INTAC: a high-resolution
756   INTegrated emission inventory of Air pollutants for China in 2017 [Data set], Zenodo, https://doi.org/10.5281/zenodo.10459198, 2024.
757   Wu, Q., Han, L., Li, S., Wang, S., Cong, Y., Liu, K., Lei, Y., Zheng, H., Li, G., Cai, B., and Hao, J.: Facility-Level Emissions and Synergistic
758   Control of Energy-Related Air Pollutants and Carbon Dioxide in China, Environmental Science & Technology, 57, 4504-4512,
759   10.1021/acs.est.2c07704, 2023.
760   Xiao, Q., Geng, G., Xue, T., Liu, S., Cai, C., He, K., and Zhang, Q.: Tracking PM2.5 and O3 Pollution and the Related Health Burden in
761   China 2013–2020, Environmental Science & Technology, 56, 6922-6932, 10.1021/acs.est.1c04548, 2022.
762   Xiu, A. and Pleim, J. E.: Development of a Land Surface Model. Part I: Application in a Mesoscale Meteorological Model, Journal of
763   Applied Meteorology, 40, 192-209, 10.1175/1520-0450(2001)040<0192:DOALSM>2.0.CO;2, 2001.
764   Yang, Y. and Zhao, Y.: Quantification and evaluation of atmospheric pollutant emissions from open biomass burning with multiple methods:
765   a case study for the Yangtze River Delta region, China, Atmos. Chem. Phys., 19, 327-348, 10.5194/acp-19-327-2019, 2019.
766   Yin, L., Du, P., Zhang, M., Liu, M., Xu, T., and Song, Y.: Estimation of emissions from biomass burning in China (2003–2017) based on
767   MODIS fire radiative energy data, Biogeosciences, 16, 1629-1640, 10.5194/bg-16-1629-2019, 2019.
768   Zhang, J., Liu, L., Zhao, Y., Li, H., Lian, Y., Zhang, Z., Huang, C., and Du, X.: Development of a high-resolution emission inventory of
769   agricultural machinery with a novel methodology: A case study for Yangtze River Delta region, Environmental Pollution, 266, 115075,
770   https://doi.org/10.1016/j.envpol.2020.115075, 2020.
771   Zhang, Q. and Geng, G.: Impact of clean air action on PM2.5 pollution in China, Science China Earth Sciences, 62, 1845-1846,
772   10.1007/s11430-019-9531-4, 2019.
773   Zhang, Q., Streets, D. G., Carmichael, G. R., He, K. B., Huo, H., Kannari, A., Klimont, Z., Park, I. S., Reddy, S., Fu, J. S., Chen, D., Duan,
774   L., Lei, Y., Wang, L. T., and Yao, Z. L.: Asian emissions in 2006 for the NASA INTEX-B mission, Atmos. Chem. Phys., 9, 5131-5153,
775   10.5194/acp-9-5131-2009, 2009.
776   Zhang, Q., Zheng, Y., Tong, D., Shao, M., Wang, S., Zhang, Y., Xu, X., Wang, J., He, H., Liu, W., Ding, Y., Lei, Y., Li, J., Wang, Z., Zhang,
777   X., Wang, Y., Cheng, J., Liu, Y., Shi, Q., Yan, L., Geng, G., Hong, C., Li, M., Liu, F., Zheng, B., Cao, J., Ding, A., Gao, J., Fu, Q., Huo, J.,
778   Liu, B., Liu, Z., Yang, F., He, K., and Hao, J.: Drivers of improved PM2.5 air quality in China from 2013 to 2017, Proc Natl Acad Sci U S
779   A, 116, 24463-24469, 10.1073/pnas.1907956116, 2019a.
780   Zhang, Y., Bo, X., Zhao, Y., and Nielsen, C. P.: Benefits of current and future policies on emissions of China's coal-fired power sector
781   indicated by continuous emission monitoring, Environmental Pollution, 251, 415-424, https://doi.org/10.1016/j.envpol.2019.05.021, 2019b.
782   Zhang, Y., Zhao, Y., Gao, M., Bo, X., and Nielsen, C. P.: Air quality and health benefits from ultra-low emission control policy indicated
783   by continuous emission monitoring: a case study in the Yangtze River Delta region, China, Atmos. Chem. Phys., 21, 6411-6430,
784   10.5194/acp-21-6411-2021, 2021.
785   Zhao, Y., Xia, Y., and Zhou, Y.: Assessment of a high-resolution NOX emission inventory using satellite observations: A case study of
786   southern Jiangsu, China, Atmospheric Environment, 190, 135-145, https://doi.org/10.1016/j.atmosenv.2018.07.029, 2018.
787   Zhao, Y., Zhou, Y., Qiu, L., and Zhang, J.: Quantifying the uncertainties of China's emission inventory for industrial sources: From national
788   to provincial and city scales, Atmospheric Environment, 165, 207-221, https://doi.org/10.1016/j.atmosenv.2017.06.045, 2017a.
789   Zhao, Y., Nielsen, C. P., Lei, Y., McElroy, M. B., and Hao, J.: Quantifying the uncertainties of a bottom-up emission inventory of
790   anthropogenic atmospheric pollutants in China, Atmos. Chem. Phys., 11, 2295-2308, 10.5194/acp-11-2295-2011, 2011.
791   Zhao, Y., Yuan, M., Huang, X., Chen, F., and Zhang, J.: Quantification and evaluation of atmospheric ammonia emissions with different
792   methods: a case study for the Yangtze River Delta region, China, Atmos. Chem. Phys., 20, 4275-4294, 10.5194/acp-20-4275-2020, 2020.

793 Zhao, Y., Mao, P., Zhou, Y., Yang, Y., Zhang, J., Wang, S., Dong, Y., Xie, F., Yu, Y., and Li, W.: Improved provincial emission inventory
794 and speciation profiles of anthropogenic non-methane volatile organic compounds: a case study for Jiangsu, China, Atmos. Chem. Phys.,
795 17, 7733-7756, 10.5194/acp-17-7733-2017, 2017b.
796 Zhao, Y., Qiu, L. P., Xu, R. Y., Xie, F. J., Zhang, Q., Yu, Y. Y., Nielsen, C. P., Qin, H. X., Wang, H. K., Wu, X. C., Li, W. Q., and Zhang,
797 J.: Advantages of a city-scale emission inventory for urban air quality research and policy: the case of Nanjing, a typical industrial city in
798 the Yangtze River Delta, China, Atmos. Chem. Phys., 15, 12623-12644, 10.5194/acp-15-12623-2015, 2015.
799 Zheng, B., Huo, H., Zhang, Q., Yao, Z. L., Wang, X. T., Yang, X. F., Liu, H., and He, K. B.: High-resolution mapping of vehicle emissions
800 in China in 2008, Atmospheric Chemistry and Physics, 14, 9787-9805, 10.5194/acp-14-9787-2014, 2014.
801 Zheng, B., Cheng, J., Geng, G., Wang, X., Li, M., Shi, Q., Qi, J., Lei, Y., Zhang, Q., and He, K.: Mapping anthropogenic emissions in China
802 at 1 km spatial resolution and its application in air quality modeling, Science Bulletin, 66, 612-620, 10.1016/j.scib.2020.12.008, 2021.
803 Zheng, B., Zhang, Q., Tong, D., Chen, C., Hong, C., Li, M., Geng, G., Lei, Y., Huo, H., and He, K.: Resolution dependence of uncertainties
804 in gridded emission inventories: a case study in Hebei, China, Atmos. Chem. Phys., 17, 921-933, 10.5194/acp-17-921-2017, 2017.
805 Zheng, B., Tong, D., Li, M., Liu, F., Hong, C., Geng, G., Li, H., Li, X., Peng, L., Qi, J., Yan, L., Zhang, Y., Zhao, H., Zheng, Y., He, K.,
806 and Zhang, Q.: Trends in China's anthropogenic emissions since 2010 as the consequence of clean air actions, Atmos. Chem. Phys., 18,
807 14095-14111, 10.5194/acp-18-14095-2018, 2018.
808 Zheng, H., Cai, S., Wang, S., Zhao, B., and Hao, J.: Development of a unit-based industrial emission inventory in the Beijing–Tianjin–Hebei
809 region and resulting improvement in air quality modeling, Atmospheric Chemistry and Physics, 19, 3447-3462, 2019.
810 Zheng, J., He, M., Shen, X., Yin, S., and Yuan, Z.: High resolution of black carbon and organic carbon emissions in the Pearl River Delta
811 region, China, Science of The Total Environment, 438, 189-200, https://doi.org/10.1016/j.scitotenv.2012.08.068, 2012.
812 Zhou, Y., Zhao, Y., Mao, P., Zhang, Q., Zhang, J., Qiu, L., and Yang, Y.: Development of a high-resolution emission inventory and its
813 evaluation and application through air quality modeling for Jiangsu Province, China, Atmos. Chem. Phys., 17, 211-233, 10.5194/acp-17-
814 211-2017, 2017a.
815 Zhou, Y., Xing, X., Lang, J., Chen, D., Cheng, S., Wei, L., Wei, X., and Liu, C.: A comprehensive biomass burning emission inventory with
816 high spatial and temporal resolution in China, Atmospheric Chemistry and Physics, 17, 2839-2864, 2017b.